

Wavelet-based Edge Multiscale Parareal Algorithm for Parabolic Equations with Heterogeneous Coefficients

Guanglian Li* and Jiuhua Hu†

February 28, 2022

Abstract

We propose in this paper the Wavelet-based Edge Multiscale Parareal (WEMP) Algorithm to efficiently solve parabolic equations with heterogeneous coefficients. This algorithm combines the advantages of multiscale methods that can deal with heterogeneity in the spacial domain effectively, and the strength of parareal algorithms for speeding up time evolution problems when sufficient processors are available. We derive the convergence rate of this algorithm in terms of the mesh size in the spatial domain, the level parameter used in the multiscale method, the coarse-scale time step and the fine-scale time step. Several numerical tests are presented to demonstrate the performance of our algorithm, which verify our theoretical results perfectly.

Keywords: multiscale, heterogeneous, edge, wavelets, parareal, parabolic

1 Introduction

We consider in this paper a new efficient multiscale parareal algorithm for parabolic problems with heterogeneous coefficients. We first formulate the heterogeneous parabolic problems to present our new multiscale methods. Let $D \subset \mathbb{R}^d$ ($d = 1, 2, 3$) be an open bounded Lipschitz domain. We seek a function $u(\cdot, t) \in V := H_0^1(D)$ such that

$$\begin{aligned} \frac{\partial u}{\partial t} - \nabla \cdot (\kappa \nabla u) &= f && \text{in } D \times (0, T], \\ u(\cdot, 0) &= u_0 && \text{in } D, \\ u &= 0 && \text{on } \partial D \times [0, T], \end{aligned} \tag{1.1}$$

where the force term $f \in L^2([0, T]; \dot{H}^2(D))$ satisfying $\partial_t f \in L^2([0, T]; L^2(D))$, the initial data $u_0 \in \dot{H}^3(D) \cap H_0^1(D)$ and the permeability coefficient $\kappa \in C^\infty(D)$ with $\alpha \leq \kappa(x) \leq \beta$ almost everywhere for some lower bound $\alpha > 0$ and upper bound $\beta > \alpha$. Furthermore, the compatibility condition holds: $f(\cdot, 0) + \nabla \cdot (\kappa \nabla u_0) \in H_0^1(D)$. Here, $\dot{H}^3(D) \subset L^2(D)$ is a Hilbert space to be defined in Section 2. We denote by $\Lambda := \frac{\beta}{\alpha}$ the ratio of these bounds, which reflects the contrast of the coefficient κ . To simplify the

*Corresponding author. Bernoulli Institute, University of Groningen, Nejinborgh 9, 9747 AG, Groningen, The Netherlands. (lotusli0707@gmail.com, guanglian.li@rug.nl). GL acknowledges the support from the Royal Society (London, United Kingdom) through a Newton international fellowship.

†Department of Mathematics, Texas A&M University, College Station, TX 77843-3368, USA. (E-mail: jhu@math.tamu.edu)

notation, let $I := [0, T]$. Note that the existence of multiple scales in the coefficient κ renders directly solving Problem (1.1) challenging, since resolving the problem to the finest scale would incur huge computational cost.

The accurate description of many important applications, e.g., composite materials, porous media and reservoir simulation, involves mathematical models with heterogeneous coefficients. In order to adequately describe the intrinsic complex properties in practical scenarios, the heterogeneous coefficients can have both multiple inseparable scales and high-contrast. Due to this disparity of scales, the classical numerical treatment becomes prohibitively expensive and even intractable for many multiscale applications. Nonetheless, motivated by the broad spectrum of practical applications, a large number of multiscale model reduction techniques, e.g., multiscale finite element methods (MsFEMs), heterogeneous multiscale methods (HMMs), variational multiscale methods, flux norm approach, generalized multiscale finite element methods (GMsFEMs) and localized orthogonal decomposition (LOD), have been proposed in the literature [19, 7, 20, 4, 8, 29, 23] over the last few decades. They have achieved great success in the efficient and accurate simulation of heterogeneous problems. Recently, a so-called Wavelet-based Edge Multiscale Finite Element Method (WEMsFEM), c.f. Algorithm 1, was proposed within the framework of GMsFEMs [8] that facilitates deriving a rigorous convergence rate with merely mild assumptions [22, 14, 15]. The main idea of this method is to utilize wavelets as the basis functions over the coarse edges, and transform the approximate rate over the edges to the convergence rate in each local region. Then the Partition of Unity Method (PUM) [30] is applied to derive the global convergence rate. The motivation for using wavelets as the ansatz space is that due to the existence of heterogeneity, the solution has a low regularity, and wavelets are known to be efficient in approximating functions with low regularity. We will apply this method in this paper to handle the heterogeneity in the spatial domain D .

Furthermore, motivated by the great demand for an efficient solver with high accuracy as well as a reasonable computing time in many practical applications, e.g., financial mathematics [3], fluid mechanics and fluid-structure interaction [11, 12, 13], oceanography [25], chemistry [27, 5] and quantum chemistry [28], and the increasing computational capacity of current computers, a variety of efficient numerical schemes exploiting parallel computing architectures emerge during the last few decades. Among them, the parareal algorithm is one of the most popular and success algorithms. The parareal algorithm facilitates speeding up the numerical simulation of the solutions to time dependent equations on the condition of sufficient processors [2], which is an iterative solver based on a cheap inaccurate sequential coarse-scale time solver and expensive accurate fine-scale time solvers that can be performed in parallel. It was introduced by Lions, Mayday and Turinici [24]. The convergence analysis is studied for nonlinear system of ordinary differential equations and partial differential equations [16, 3]. Recently, new parareal algorithms are developed to solve problems involving discontinuous right-hand sides [17, 18]. Coupling of parareal algorithm and some other techniques has been developed in many literatures, see [10, 6, 21, 1]. One of these is the coupling of parareal algorithm and model reduction techniques. In [21], a micro-macro parareal algorithm for the time-parallel integration of multiscale-in-time systems is introduced to solve singularly perturbed ordinary differential equations. One contribution of this paper is that the fast variables are eliminated from the coarse propagator, therefore, the associated algorithm only evolves the slow variables. A new coupling strategy for the parareal algorithm with multiscale integrators is introduced in [1].

In this paper, we incorporate the parareal algorithm into WEMsFEM to numerically calculate the time evolution problems efficiently. This new algorithm is called WEMP Algorithm, c.f. Algorithm 2. This algorithm is divided into two steps: a multiscale space $V_{\text{ms},\ell}^{\text{EW}}$ based on WEMsFEM with ℓ as the wavelets level parameter is constructed in the first step, and then we apply the parareal algorithm by using $V_{\text{ms},\ell}^{\text{EW}}$ as the ansatz space in the second step to obtain the solution more efficiently. The convergence rate of this

algorithm is studied in Theorem 5.1. We proved

$$\begin{aligned} \|u(\cdot, T^n) - U_k^n\|_{L^2(D)} &\lesssim (H + 2^{-\ell/2} \|\kappa\|_{L^\infty(\mathcal{F}_H)}) H |u_0|_2 + \delta t \left(|u_0|_3 + \|f\|_{L^2(I; \dot{H}^2(D))} + \|\partial_t f\|_{L^2(I; L^2(D))} \right) \\ &\quad + \left(\frac{1}{T^{n-1}} \right)^{k+1} \frac{1}{k!} (\Delta T)^{k+1} \|u_0\|_{L^2(D)}, \end{aligned}$$

where $u(\cdot, T^n)$ and U_k^n are the numerical solution at $T^n = n \times \Delta T$ for $n = 2, \dots$ derived from the backward Euler conforming Galerkin method and WEMP algorithm. The notations ΔT and δt represent for the coarse time step size and fine time step size, respectively. H , ℓ and k are the space domain mesh size, the level parameter and iteration number. This implies that taking $\ell = \mathcal{O}(|\log H|)$ and $k = \mathcal{O}(|\log \delta t / \log \Delta T|)$, we recover $\mathcal{O}(H^2 + \delta t)$ error, which actually is the error for the backward Euler conforming Galerkin method. Furthermore, the singularity of the solution for $t \rightarrow 0$ is reflected in the coefficient of the last term, namely, $\left(\frac{1}{T^{n-1}} \right)^{k+1}$.

To demonstrate the performance of our proposed algorithm we present several numerical tests using backward Euler and Crank-Nicolson schemes for the fine time step solver, respectively. Our numerical tests indicate similar convergence as derived in the theoretical results. Furthermore, we take different coarse time steps and observe similar convergence behavior.

The paper is organized as follows. We present the basics on the discretization of Problem (1.1) and the framework of Generalized Multiscale Finite Element Methods (GMsFEMs) in Section 2. Then in Section 3, we present the construction of multiscale space $V_{\text{ms}, \ell}^{\text{EW}}$ by WEMsFEMs and its approximation properties. Our main proposed algorithm is presented in Section 4. Its convergence rate is derived in Section 5. Extensive numerical tests are presented in Section 6. Finally, we complete our paper with concluding remarks in Section 7.

2 Problem setting

We present in this section the discretization of problem (1.1). Firstly, we define the Hilbert space $\dot{H}^s(D)$, which is analogous to [31, Chapter 3].

Let $\{(\lambda_m, \phi_m)\}_{m=1}^\infty$ be the eigenpairs of the following eigenvalue problems with the eigenvalues arranged in a nondecreasing order,

$$\begin{aligned} \mathcal{L}\phi_m &:= -\nabla \cdot (\kappa \nabla \phi_m) = \lambda_m \phi_m && \text{in } D \\ \phi_m &= 0 && \text{on } \partial D. \end{aligned}$$

Note that the eigenfunctions $\{\phi_m\}_{m=1}^\infty$ form an orthonormal basis in $L^2(D)$, and consequently, each $v \in L^2(D)$ admits the representation $v = \sum_{m=1}^\infty (v, \phi_m)_D \phi_m$ with $(\cdot, \cdot)_D$ being the inner product in $L^2(D)$. The Hilbert space $\dot{H}^s(D) \subset L^2(D)$ is defined by

$$\dot{H}^s(D) = \{v \in L^2(D) : \sum_{m=1}^\infty \lambda_m^s |(v, \phi_m)_D|^2 < \infty\}. \quad (2.1)$$

The associated norm in $\dot{H}^s(D)$ is $|v|_s = (\sum_{m=1}^\infty \lambda_m^s |(v, \phi_m)_D|^2)^{1/2}$.

Remark 2.1. Since the initial data $u_0 \in \dot{H}^3(D) \cap H_1^0(D)$, we obtain

$$\|\mathcal{L}u_0\|_{L^2(D)} = |u_0|_2. \quad (2.2)$$

Indeed, u_0 allows the expression

$$u_0 = \sum_{m=1}^{\infty} (u_0, \phi_m)_D \phi_m.$$

Taking $L^2(D)$ -norm after Operating \mathcal{L} on both sides and utilize the definition (2.1), we obtain the desired assertion (2.2).

Next we recap the regularity results to problem (1.1), which can be found, e.g., in [9]:

$$\sum_{j=0}^2 \int_0^T \left| \frac{\partial^j u}{\partial t^j} \right|_{2(1-j)+2}^2 dt \lesssim |u_0|_3^2 + \|f\|_{L^2(I; \dot{H}^2(D))}^2 + \|\partial_t f\|_{L^2(I; L^2(D))}^2. \quad (2.3)$$

To discretize problem (1.1), we first introduce fine and coarse grids. Let \mathcal{T}_H be a regular partition of the domain D into finite elements (triangles, quadrilaterals, tetrahedral, etc.) with a mesh size H . We refer to this partition as coarse grids, and its elements as the coarse elements. Then each coarse element is further partitioned into a union of connected fine grid blocks. The fine-grid partition is denoted by \mathcal{T}_h with h being its mesh size. Let \mathcal{F}_h (or \mathcal{F}_H) be the collection of all edges in \mathcal{T}_h (or \mathcal{T}_H). Over the fine mesh \mathcal{T}_h , let V_h be the conforming piecewise linear finite element space:

$$V_h := \{v \in V : v|_E \in \mathcal{P}_1(E) \text{ for all } E \in \mathcal{T}_h\},$$

where $\mathcal{P}_1(E)$ denotes the space of linear polynomials on the fine element $E \in \mathcal{T}_h$.

The time interval $I := [0, T]$ is decomposed into a sequence of coarse subintervals $[T^n, T^{n+1}]$ for $n = 0, 1, \dots, M_\Delta$ of size ΔT with $\Delta T := T/M_\Delta$ for some $M_\Delta \in \mathbb{N}_+$ and $T^0 := 0$. Each coarse time interval $[T^n, T^{n+1}]$ is further discretized with a fine time step δt . Let $t_n = n \times \delta t$ for $n = 0, 1, \dots, M_\delta$ with $M_\delta := T \times \delta t^{-1}$. Note that $\Delta T \gg \delta t$. To simplify the notations, backward Euler method is utilized to discretize the time variable, and we use conforming Galerkin method for the discretization in the spatial variable throughout this paper. Then the fine-scale solution $u_h^n \in V_h$ for $n = 1, 2, \dots, M_\delta$ satisfies

$$\begin{cases} \left(\frac{u_h^n - u_h^{n-1}}{\delta t}, v_h \right)_D + a(u_h^n, v_h) = (f(\cdot, t_n), v_h)_D & \text{for all } v_h \in V_h, \\ u_h^0 = I_h u_0. \end{cases} \quad (2.4)$$

Here, the bilinear form $a(\cdot, \cdot)$ on $V \times V$ is defined by

$$a(v_1, v_2) := \int_D \kappa \nabla v_1 \cdot \nabla v_2 dx \text{ for all } v_1, v_2 \in V.$$

I_h is a proper projection from V to V_h . Furthermore, we define the energy norm $\|v\|_{H_\kappa^1(D)} := \sqrt{a(v, v)}$ for all $v \in V$.

The fine-scale solution u_h^n will serve as a reference solution in Section 6. Note that due to the presence of multiple scales in the coefficient κ , the fine-scale mesh size h should be commensurate with the smallest scale and thus it can be very small in order to obtain an accurate solution. This necessarily involves huge computational complexity, and more efficient methods are in great demand.

In this work, we are concerned with flow problems with high-contrast heterogeneous coefficients, which involve multiscale permeability fields, e.g., permeability fields with vugs and faults, and furthermore, can be parameter-dependent, e.g., viscosity. Under such scenario, the computation of the fine-scale solution u_h

is vulnerable to high computational complexity, and one has to resort to multiscale methods. The GMsFEM has been extremely successful for solving multiscale flow problems, which we briefly recap below.

The GMsFEM aims at solving Problem (1.1) on the coarse mesh \mathcal{T}_H cheaply, which, meanwhile, maintains a certain accuracy compared to the fine-scale solution u_h . To describe the GMsFEM, we need a few notations. The vertices of \mathcal{T}_H are denoted by $\{O_i\}_{i=1}^N$, with N being the total number of coarse nodes. The coarse neighborhood associated with the node O_i is denoted by

$$\omega_i := \bigcup \{K_j \in \mathcal{T}_H : O_i \in \overline{K_j}\}. \quad (2.5)$$

We refer to Figure 1 for an illustration of neighborhoods and elements subordinated to the coarse discretization \mathcal{T}_H . Throughout, we use ω_i to denote a coarse neighborhood. Furthermore, let $\mathcal{F}_h(\partial\omega_i)$ (or $\mathcal{F}_H(\partial\omega_i)$) be the restriction of \mathcal{F}_h on $\partial\omega_i$ (or \mathcal{F}_H on $\partial\omega_i$).

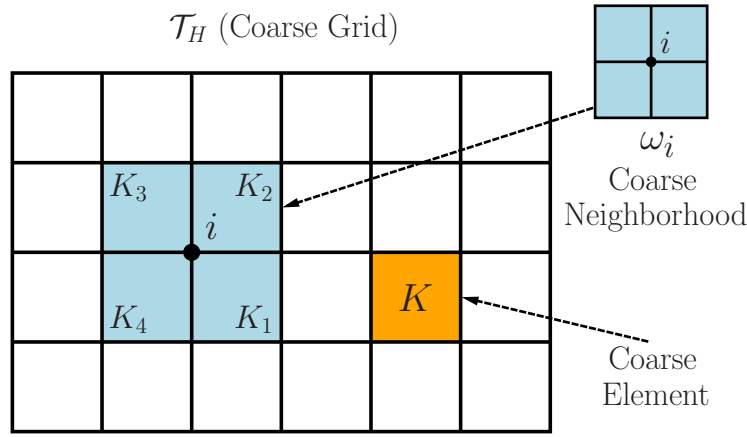


Figure 1: Illustration of a coarse neighborhood and coarse element.

Next, we outline the GMsFEM with a conforming Galerkin (CG) formulation. Let $1 \leq i \leq N$ be a certain coarse node. Note that ω_i is the support of the multiscale basis functions to be identified, and $\ell_i \in \mathbb{N}_+$ is the number of those multiscale basis functions associated with ω_i . They are denoted as $\psi_k^{\omega_i}$ for $k = 1, \dots, \ell_i$. Throughout, the subscript i denotes the i -th coarse node or coarse neighborhood. Generally, the GMsFEM utilizes multiple basis functions per coarse neighborhood ω_i , and the index k represents the numbering of these basis functions. In turn, the CG multiscale solution u_{ms} is sought as $u_{\text{ms}} = \sum_{i=1}^N \sum_{k=1}^{\ell_i} c_k^i \psi_k^{\omega_i}$. Once the basis functions $\psi_k^{\omega_i}$ are identified, the multiscale solution $u_{\text{ms}}^n \in V_{\text{ms}}$ for $n = 1, \dots, M_\delta$ satisfies

$$\begin{cases} \left(\frac{u_{\text{ms}}^n - u_{\text{ms}}^{n-1}}{\delta t}, v_{\text{ms}} \right)_D + a(u_{\text{ms}}^n, v_{\text{ms}}) = (f(\cdot, t_n), v_{\text{ms}})_D & \text{for all } v_{\text{ms}} \in V_{\text{ms}}, \\ u_{\text{ms}}^0 = I_{\text{ms}} u_0, \end{cases} \quad (2.6)$$

where V_{ms} denotes the multiscale space spanned by these multiscale basis functions and I_{ms} is a projection operator from V to V_{ms} .

Note that we need to build the multiscale space V_{ms} to solve for u_{ms}^n from (2.6) for $n = 1, \dots, M_\delta$. The construction of V_{ms} will be presented in Section 3. Note also that we need a very tiny fine-scale

time step δt to guarantee a reasonable approximation property of u_{ms}^n to $u(\cdot, t_n)$ for $n = 1, \dots, M_\delta$ due to, e.g., the singularity of the solution $u(\cdot, t)$ at $t = 0$ when the source term f fails to belong to certain smooth functional space. Consequently, the computational complexity of the multiscale method (2.6) can be extremely expensive. For this reason, we present in Section 4 a multiscale algorithm incorporated with the parareal algorithm to reduce further this part of computational cost.

We end this section with assumptions on the permeability field κ :

Assumption 2.1 (Structure of D and κ). *Let D be a domain with a $C^{1,\alpha}$ ($0 < \alpha < 1$) boundary ∂D , and $\{D_i\}_{i=1}^m \subset D$ be m pairwise disjoint strictly convex open subsets, each with a $C^{1,\alpha}$ boundary $\Gamma_i := \partial D_i$, and denote $D_0 = D \setminus \bigcup_{i=1}^m \overline{D_i}$. Let the permeability coefficient κ be piecewise regular function defined by*

$$\kappa = \begin{cases} \eta_i(x) & \text{in } D_i, \\ 1 & \text{in } D_0. \end{cases} \quad (2.7)$$

Here $\eta_i \in C^\mu(\bar{D}_i)$ with $\mu \in (0, 1)$ for $i = 1, \dots, m$. Denote $\eta_{\min} := \min_i \{ \min_{x \in D_i} \{ \eta_i(x) \} \} \geq 1$ and $\eta_{\max} := \max_i \{ \|\eta_i\|_{C_0(D_i)} \}$.

3 Multiscale space construction

This section is concerned with the construction of the multiscale space by means of the Wavelet-based Edge Multiscale Finite Element Methods (WEMsFEM) [22, 15].

The algorithm is presented in Algorithm 1. Given the level parameter $\ell \in \mathbb{N}$, and the type of wavelets on each edge of the coarse neighborhood ω_i , one can obtain the local multiscale space $V_{i,\ell}$ on ω_i by solving $2^{\ell+2}$ local problems as in Step 2. In Step 3, we can use these local multiscale space to build the global multiscale space $V_{\text{ms},\ell}^{\text{EW}}$ by multiplying the partition of unity functions χ_i . Finally, we can solve the multiscale problem (2.6) using this global multiscale space.

To this end, we begin with an initial coarse space $V_0^{\text{init}} = \text{span}\{\chi_i\}_{i=1}^N$. The functions χ_i are the standard multiscale basis functions on each coarse element $K \in \mathcal{T}_H$ defined by

$$\begin{aligned} -\nabla \cdot (\kappa(x) \nabla \chi_i) &= 0 & \text{in } K, \\ \chi_i &= g_i & \text{on } \partial K, \end{aligned} \quad (3.1)$$

where g_i is affine over ∂K with $g_i(O_j) = \delta_{ij}$ for all $i, j = 1, \dots, N$. Recall that $\{O_j\}_{j=1}^N$ are the set of coarse nodes on \mathcal{T}_H . Next we define the weighted coefficient:

$$\tilde{\kappa} = H^2 \kappa \sum_{i=1}^N |\nabla \chi_i|^2. \quad (3.2)$$

Furthermore, let $\tilde{\kappa}^{-1}$ be defined by

$$\tilde{\kappa}^{-1}(x) := \begin{cases} \tilde{\kappa}^{-1}, & \text{when } \tilde{\kappa}(x) \neq 0, \\ 1, & \text{otherwise.} \end{cases} \quad (3.3)$$

Algorithm 1 Wavelet-based Edge Multiscale Finite Element Method (WEMsFEM)

Input: The level parameter $\ell \in \mathbb{N}$; coarse neighborhood ω_i and its four coarse edges $\Gamma_{i,k}$ with $k = 1, 2, 3, 4$, i.e., $\cup_{k=1}^4 \Gamma_{i,k} = \partial\omega_i$; the subspace $V_{\ell,k} \subset L^2(\Gamma_{i,k})$ up to level ℓ on each coarse edge $\Gamma_{i,k}$.

Output: Multiscale solution $u_{\text{ms},\ell}^{\text{EW}}$.

- 1: Denote $V_{i,\ell} := \oplus_{k=1}^4 V_{\ell,k}$. Then the number of basis functions in $V_{i,\ell}$ is $4 \times 2^\ell = 2^{\ell+2}$. Denote these basis functions as v_k for $k = 1, \dots, 2^{\ell+2}$.
 - 2: Calculate local multiscale basis $\mathcal{L}_i^{-1}(v_k)$ for all $k = 1, \dots, 2^{\ell+2}$. Here, $\mathcal{L}_i^{-1}(v_k) := v$ satisfies:
$$\begin{cases} \mathcal{L}_i v := -\nabla \cdot (\kappa \nabla v) = 0 & \text{in } \omega_i, \\ v = v_k & \text{on } \partial\omega_i. \end{cases}$$
 - 3: Solve one local problem.
$$\begin{cases} -\nabla \cdot (\kappa \nabla v^i) = \frac{\tilde{\kappa}}{\int_{\omega_i} \tilde{\kappa} dx} & \text{in } \omega_i, \\ -\kappa \frac{\partial v^i}{\partial n} = |\partial\omega_i|^{-1} & \text{on } \partial\omega_i. \end{cases}$$
 - 4: Build global multiscale space. $V_{\text{ms},\ell}^{\text{EW}} := \text{span}\{\chi_i \mathcal{L}_i^{-1}(v_k), \chi_i v^i : 1 \leq i \leq N, 1 \leq k \leq 2^{\ell+2}\}$.
 - 5: Solve for (2.6) by conforming Galerkin method in $V_{\text{ms},\ell}^{\text{EW}}$ to obtain $u_{\text{ms},\ell}^{\text{EW},n}$ for $n = 1, \dots, M_\delta$.
-

In the following, we define the $L^2(\partial\omega_i)$ -orthogonal projection $\mathcal{P}_{i,\ell}$ onto the local multiscale space up to level ℓ by $\mathcal{P}_{i,\ell} : L^2(\partial\omega_i) \rightarrow V_{i,\ell}$ satisfying

$$\mathcal{P}_{i,\ell}(v) := \sum_{j=1}^{2^{\ell+2}} (v, \psi_j)_{\partial\omega_i} \mathcal{L}_i^{-1}(\psi_j) \quad \text{for all } v \in L^2(\partial\omega_i). \quad (3.4)$$

Here, we denote ψ_j for $j = 1, \dots, 2^{\ell+2}$ as the Haar wavelets defined on the four edges of ω_i of level ℓ and the local operator \mathcal{L}_i is defined as in Algorithm 1.

Let $\mathcal{L} := -\nabla \cdot (\kappa \nabla \cdot)$ be the elliptic operator defined on $H_\kappa^1(D)$, and \mathcal{P}_ℓ be the projection onto the multiscale space $V_{\text{ms},\ell}^{\text{EW}}$ given by

$$\mathcal{P}_\ell(v) := \sum_{i=1}^N \chi_i \mathcal{P}_{i,\ell}(v) \quad \text{for all } v \in H_\kappa^1(D). \quad (3.5)$$

Then [14, Proposition 5.2] implies that for any $v \in L^2(D) \cap L_{\tilde{\kappa}-1}^2(D)$, it holds

$$\|\mathcal{L}^{-1}v - \mathcal{P}_\ell(\mathcal{L}^{-1}v)\|_{H_\kappa^1(D)} \lesssim H \|\tilde{\kappa}\|_{L^\infty(D)}^{1/2} \|v\|_{L_{\tilde{\kappa}-1}^2(D)} + 2^{-\ell/2} \|\kappa\|_{L^\infty(\mathcal{F}_H)} \|v\|_{L^2(D)}. \quad (3.6)$$

Furthermore, the following result holds.

Lemma 3.1 (Approximation properties of \mathcal{P}_ℓ). *There holds*

$$\forall v \in L^2(D) : \quad \|\mathcal{L}^{-1}v - \mathcal{P}_\ell(\mathcal{L}^{-1}v)\|_{L^2(D)} \lesssim (H + 2^{-\ell/2} \|\kappa\|_{L^\infty(\mathcal{F}_H)}) H \|v\|_{L^2(D)}. \quad (3.7)$$

Proof. This assertion can be derived from the proofs of [14, Lemma 5.1 and Proposition 5.2]. \square

4 Wavelet-based Edge Multiscale Parareal Algorithm

We construct in this section the Wavelet-based Edge Multiscale Parareal (WEMP) Algorithm, cf. Algorithm 2, which is divided into two main steps. In the first step, the multiscale space $V_{\text{ms},\ell}^{\text{EW}}$ for $\ell \in \mathbb{N}_+$ is built based on Section 3. This multiscale space serves as the trial space and test space for our conforming Galerkin method, cf. (2.6). Then the parareal algorithm is utilized in the second step to solve the problem.

We first recap a few terminologies commonly appeared in parareal algorithm.

The one step coarse solver on the time domain $(0, T)$ is

$$\begin{aligned} U^{n+1} &= E_{\Delta}(T^n, U^n), \quad U^0 = I_h u_0, \\ U_{\text{ms},\ell}^{n+1} &= E_{\Delta}^{\text{ms},\ell}(T^n, U_{\text{ms},\ell}^n), \quad U_{\text{ms},\ell}^0 = \mathcal{P}_{\ell} u_0, \end{aligned} \quad (4.1)$$

which yields U^{n+1} (or $U_{\text{ms},\ell}^{n+1}$) as a coarse approximation to $u(\cdot, T^{n+1})$, provided with an approximation U^n (or $U_{\text{ms},\ell}^n$) of $u(\cdot, T^n)$. In matrix form, it reads

$$\begin{aligned} U^{n+1} &= (M + \Delta T \times A)^{-1} M (U^n + \Delta T \times F^{n+1}), \\ U_{\text{ms},\ell}^{n+1} &= \Phi_{\text{ms},\ell} (\Phi_{\text{ms},\ell}^T M \Phi_{\text{ms},\ell} + \Delta T \times \Phi_{\text{ms},\ell}^T A \Phi_{\text{ms},\ell})^{-1} \Phi_{\text{ms},\ell}^T M (U_{\text{ms},\ell}^n + \Delta T \times F^{n+1}). \end{aligned}$$

Here, A and M are the mass matrices and stiffness matrices corresponding to the discretization of the elliptic operator $-\nabla \cdot (\kappa \nabla \cdot)$ in the finite element space $V_h := \text{span}\{\phi_1, \dots, \phi_{\text{dof}_h}\}$. Here, dof_h denotes the dimension of V_h . $(F^{n+1})_i := \int_D f(\cdot, t_{n+1}) \phi_i dx$ for all $i = 1, \dots, \text{dof}_h$. $\Phi_{\text{ms},\ell}$ denotes a matrix with columns composed of the coefficients of multiscale basis functions in $V_{\text{ms},\ell}^{\text{EW}}$ in the finite element space V_h .

The one step fine solver

$$\begin{aligned} \psi &= \mathcal{F}_{\delta}(s, \sigma, \phi), \\ \psi_{\text{ms},\ell} &= \mathcal{F}_{\delta}^{\text{ms},\ell}(s, \sigma, \phi), \end{aligned} \quad (4.2)$$

yields an approximation $\psi(\cdot, s + \sigma)$ (or $\psi_{\text{ms},\ell}(\cdot, s + \sigma)$) to the solution $u(\cdot, s + \sigma)$ with the initial condition $\psi(\cdot, s) = \phi$ (or $\psi_{\text{ms},\ell}(\cdot, s) = \mathcal{P}_{\ell}(\phi)$) and a uniform discrete time step δ for all $s \in (0, T)$ and $\sigma \in (0, T - s)$ in the infinite dimensional space V (or in the ansatz space $V_{\text{ms},\ell}^{\text{EW}}$) with $s/\delta t \in \mathbb{N}_+$.

We also define the semi-discretization in space solver

$$u_{\text{ms},\ell}(\cdot, s + \sigma) = \mathcal{F}^{\text{ms},\ell}(s, \sigma, \phi), \quad (4.3)$$

which yields an approximation $u_{\text{ms},\ell}(\cdot, s + \sigma)$ to the solution $u(\cdot, s + \sigma)$ with initial condition $u_{\text{ms},\ell}(\cdot, s) = \mathcal{P}_{\ell}(\phi)$ for all $s \in (0, T)$, $\sigma \in (0, T - s)$ in the ansatz space $V_{\text{ms},\ell}^{\text{EW}}$. We will denote $\bar{E}_{\Delta}^{\text{ms},\ell}(T^n, U_{\text{ms},\ell}^n)$ as the one step coarse solver with $f = 0$. We will define $\bar{\mathcal{F}}^{\text{ms},\ell}(s, \sigma, \phi)$ and $\bar{\mathcal{F}}_{\delta}^{\text{ms},\ell}(s, \sigma, \phi)$ analogously.

Note that the cheap multiscale coarse solver $E_{\Delta}^{\text{ms},\ell}$ is sequentially utilized over the global time interval I to provide a rough approximation to $u(\cdot, T^{n+1})$, while the expensive accurate multiscale fine solver $\mathcal{F}_{\delta}^{\text{ms},\ell}$ is applied in each subinterval $[T^n, T^{n+1}]$ for $n = 0, 1, \dots, M_{\Delta} - 1$ independently. This local fine solver will embed more detailed information to the approximation of $u(\cdot, T^{n+1})$, which usually differs from the one obtained from the global coarse solver. In the process of parareal algorithm, a correction operator is very important to improve the approximation to $u(\cdot, T^{n+1})$ based on the discrepancy between the coarse solver and fine solver, which is defined by

$$\mathcal{S}(T^n, U_{\text{ms},\ell}^n) := \mathcal{F}_{\delta}^{\text{ms},\ell}(T^n, \Delta T, U_{\text{ms},\ell}^n) - E_{\Delta}^{\text{ms},\ell}(T^n, U_{\text{ms},\ell}^n) \quad \text{and} \quad U_{\text{ms},\ell}^0 = \mathcal{P}_{\ell} u_0$$

for all $n = 0, 1, \dots, M_\Delta - 1$.

Now we are ready to present our main algorithm, i.e., Algorithm 2. To obtain a good approximation to the solution of (1.1) at discrete time points $\{T^n\}$ for $n = 1, \dots, M_\Delta$, we first construct a proper multiscale space $V_{\text{ms},\ell}^{\text{EW}}$ based on the WEMsFEM, i.e., Algorithm 1, which corresponds to Steps 1 to 3. This allows one to solve (2.6) using the constructed multiscale space $V_{\text{ms},\ell}^{\text{EW}}$ and obtain an intermediate solution $u_{\text{ms},\ell}^{\text{EW},n}$ with certain accuracy depending on the spatial coarse mesh size H and level parameter ℓ . This solution will only be utilized in the convergence analysis.

In order to further reduce the computational cost, we apply the parareal algorithm in the following. Given the iteration parameter k , we apply the global coarse solver (4.1) in Step 6 to obtain U_k^{n+1} , which is an approximation to the intermediate solution $u_{\text{ms},\ell}^{\text{EW},n+1}$ from Algorithm 1. Using the coarse solution U_k^n as the initial condition, the fine solver (4.2) subsequently is used to calculate the fine solution u_k^{n+1} in parallel on each local time subinterval $[T^n, T^{n+1}]$. Then we calculate the discrepancy between the coarse solution and the fine solution in Step 8 on each discrete coarse time point T^n for $n = 1, 2, \dots, M_\Delta$, and denote it as $\mathcal{S}(T^{n-1}, U_k^{n-1})$. Subsequently, this jump term is utilized in Step 9 to update the coarse solution via the global coarse solver (4.1). This process will be performed iteratively until certain tolerance on the jump terms is satisfied.

5 Convergence study

We present in this section the convergence analysis for Algorithm 2. To this end, we first prove the boundedness and Lipschitz continuity properties of the coarse solver $E_\Delta^{\text{ms},\ell}$ and the jump operator \mathcal{S} in the multiscale space $V_{\text{ms},\ell}^{\text{EW}}$:

Lemma 5.1. *For all $n \in \{1, \dots, M_\Delta - 1\}$, the following properties hold.*

1. *The one step coarse solver $E_\Delta^{\text{ms},\ell}$ is Lipschitz in $V_{\text{ms},\ell}^{\text{EW}}$. For all $v_1, v_2 \in V_{\text{ms},\ell}^{\text{EW}}$, there holds*

$$\|E_\Delta^{\text{ms},\ell}(T^n, v_1) - E_\Delta^{\text{ms},\ell}(T^n, v_2)\|_{L^2(D)} \leq \|v_1 - v_2\|_{L^2(D)}.$$

2. *The jump operator \mathcal{S} is an approximation of order 1 with Lipschitz regularity. For all $v_1, v_2 \in V_{\text{ms},\ell}^{\text{EW}}$, there holds*

$$\|\mathcal{S}(T^n, v_1) - \mathcal{S}(T^n, v_2)\|_{L^2(D)} \leq \frac{1}{T^n T^{n+1}} (\Delta T)^2 \|v_1 - v_2\|_{L^2(D)}. \quad (5.1)$$

Proof. 1. Let $e_{\text{ms}}^{n+1} := E_\Delta^{\text{ms},\ell}(T^n, v_1) - E_\Delta^{\text{ms},\ell}(T^n, v_2)$, then it holds

$$\forall w_{\text{ms}} \in V_{\text{ms},\ell}^{\text{EW}} : \int_D e_{\text{ms}}^{n+1} w_{\text{ms}} \, dx + \Delta T \int_D \kappa \nabla e_{\text{ms}}^{n+1} \cdot \nabla w_{\text{ms}} \, dx = \int_D (v_1 - v_2) w_{\text{ms}} \, dx.$$

Choosing $w_{\text{ms}} := e_{\text{ms}}^{n+1}$ leads to

$$\|e_{\text{ms}}^{n+1}\|_{L^2(D)}^2 + \Delta T \|e_{\text{ms}}^{n+1}\|_{H_\kappa^1(D)}^2 = \int_D e_{\text{ms}}^{n+1} (v_1 - v_2) \, dx.$$

Finally an application of the Young's inequality proves the first assertion.

Algorithm 2 Wavelet-based Edge Multiscale Parareal (WEMP) Algorithm

Input: The initial data u_0 , the source term f ; tolerance ϵ ; the level parameter $\ell \in \mathbb{N}$; coarse neighborhood ω_i and its four coarse edges $\Gamma_{i,j}$ with $j = 1, 2, 3, 4$, i.e., $\cup_{j=1}^4 \Gamma_{i,j} = \partial\omega_i$; the subspace $V_{\ell,j}^i \subset L^2(\Gamma_{i,j})$ up to level ℓ on each coarse edge $\Gamma_{i,j}$.

Output: U .

- 1: Denote $V_{i,\ell} := \oplus_{k=1}^4 V_{\ell,k}^i$. Then the number of basis functions in $V_{i,\ell}$ is $4 \times 2^\ell = 2^{\ell+2}$. Denote these basis functions as v_k for $k = 1, \dots, 2^{\ell+2}$.
- 2: Calculate local multiscale basis $\mathcal{L}_i^{-1}(v_m)$ for all $m = 1, \dots, 2^{\ell+2}$. Here, $\mathcal{L}_i^{-1}(v_m) := v$ satisfies:
$$\begin{cases} \mathcal{L}_i v := -\nabla \cdot (\kappa \nabla v) = 0 & \text{in } \omega_i, \\ v = v_m & \text{on } \partial\omega_i. \end{cases}$$
- 3: Build global multiscale space. $V_{\text{ms},\ell}^{\text{EW}} := \text{span}\{\chi_i \mathcal{L}_i^{-1}(v_k), \chi_i v^i : 1 \leq i \leq N, 1 \leq k \leq 2^{\ell+2}\}$.
- 4: $k = 0$, err = 1.
- 5: **while** err > ϵ **do**
- 6: Compute U_k^{n+1} for $n = 0, \dots, M_\Delta - 1$:

$$\begin{aligned} U_k^{n+1} &= E_\Delta^{\text{ms},\ell}(T^n, U_k^n), \\ U_k^0 &= \mathcal{P}_\ell u_0. \end{aligned}$$

- 7: Compute u_k^{n+1} for $n = 0, \dots, M_\Delta - 1$ on each local time subinterval $[T^n, T^{n+1}]$:

$$u_k^{n+1} = \mathcal{F}_\delta^{\text{ms},\ell}(T^n, \Delta T, U_k^n).$$

- 8: Compute the jumps for $n = 1, \dots, M_\Delta$:

$$\mathcal{S}(T^{n-1}, U_k^{n-1}) := u_k^n - U_k^n.$$

- 9: Compute the corrected coarse solutions U_{k+1}^{n+1} for $n = 0, \dots, M_\Delta - 1$:

$$\begin{aligned} U_{k+1}^{n+1} &= \mathcal{S}(T^n, U_k^n) + E_\Delta^{\text{ms},\ell}(T^n, U_{k+1}^n), \\ U_{k+1}^0 &= \mathcal{P}_\ell u_0. \end{aligned}$$

- 10: Calculate the error:

$$\text{err} := 1/M_\Delta \sum_{n=1}^{M_\Delta} \|U_{k+1}^n - U_k^n\|_{\ell_2}.$$

$$k \leftarrow k + 1$$

- 11: **end while**

- 12: $U_n := U_k^n$ and $U := [U_0, \dots, U_{M_\Delta}]$.
-

2. To prove the second assertion, let

$$\begin{aligned}
e_{\text{ms}}^{n+1} &:= \mathcal{S}(T^n, v_1) - \mathcal{S}(T^n, v_2) \\
&= \left(\mathcal{F}_\delta^{\text{ms}, \ell}(T^n, \Delta T, v_1) - \mathcal{F}_\delta^{\text{ms}, \ell}(T^n, \Delta T, v_2) \right) - \left(E_\Delta^{\text{ms}, \ell}(T^n, v_1) - E_\Delta^{\text{ms}, \ell}(T^n, v_2) \right) \\
&= \bar{\mathcal{F}}_\delta^{\text{ms}, \ell}(T^n, \Delta T, v_1 - v_2) - \bar{E}_\Delta^{\text{ms}, \ell}(T^n, v_1 - v_2) \\
&= \left(\bar{\mathcal{F}}_\delta^{\text{ms}, \ell}(T^n, \Delta T, v_1 - v_2) - \bar{\mathcal{F}}^{\text{ms}, \ell}(T^n, \Delta T, v_1 - v_2) \right) - \left(\bar{E}_\Delta^{\text{ms}, \ell}(T^n, v_1 - v_2) \right. \\
&\quad \left. - \bar{\mathcal{F}}^{\text{ms}, \ell}(T^n, \Delta T, v_1 - v_2) \right) \\
&=: e_{\text{ms}, \delta}^{n+1} - e_{\text{ms}, \Delta}^{n+1}.
\end{aligned}$$

To estimate e_{ms}^{n+1} , we only need to derive the estimate for $e_{\text{ms}, \delta}^{n+1}$ and $e_{\text{ms}, \Delta}^{n+1}$, separately.

To this end, let $v_{\text{ms}, i}^{n+1} := v_{\text{ms}, i}(\cdot, T^{n+1}) := \mathcal{F}^{\text{ms}, \ell}(T^n, \Delta T, v_i)$ for $i = 1, 2$, we first construct the equation for $e_{\text{ms}, \Delta}^{n+1}$ by the definitions of the coarse solver (4.1) and fine solver (4.2). There holds

$$\forall w_{\text{ms}} \in V_{\text{ms}, \ell}^{\text{EW}} : \int_D e_{\text{ms}, \Delta}^{n+1} w_{\text{ms}} \, dx + \Delta T \int_D \kappa \nabla e_{\text{ms}, \Delta}^{n+1} \cdot \nabla w_{\text{ms}} \, dx = \int_D w_0 \cdot w_{\text{ms}} \, dx.$$

Here,

$$\begin{aligned}
w_0 &:= \Delta T \left(-\partial_t v_{\text{ms}, 1}|_{t=T^{n+1}} + \frac{v_{\text{ms}, 1}^{n+1} - v_1}{\Delta T} + \partial_t v_{\text{ms}, 2}|_{t=T^{n+1}} - \frac{v_{\text{ms}, 2}^{n+1} - v_2}{\Delta T} \right) \\
&= - \int_{T^n}^{T^{n+1}} (s - T^n) \partial_{ss}(v_{\text{ms}, 1} - v_{\text{ms}, 2})(\cdot, s) \, ds.
\end{aligned}$$

Note that

$$\|w_0\|_{L^2(D)} \leq \Delta T \int_{T^n}^{T^{n+1}} \|\partial_{ss}(v_{\text{ms}, 1} - v_{\text{ms}, 2})(\cdot, s)\|_{L^2(D)} \, ds.$$

An adaptation of the proof to [31, Lemma 3.2] shows

$$\|\partial_{tt}(v_{\text{ms}, 1} - v_{\text{ms}, 2})(\cdot, t)\|_{L^2(D)} \lesssim t^{-2} \|v_1 - v_2\|_{L^2(D)} \text{ for all } t > 0.$$

Consequently, we derive

$$\|w_0\|_{L^2(D)} \leq \frac{1}{T^n T^{n+1}} (\Delta T)^2 \|v_1 - v_2\|_{L^2(D)}.$$

Choosing $w_{\text{ms}} := e_{\text{ms}, \Delta}^{n+1}$ leads to

$$\left\| e_{\text{ms}, \Delta}^{n+1} \right\|_{L^2(D)}^2 + \Delta T \left\| e_{\text{ms}, \Delta}^{n+1} \right\|_{H_\kappa^1(D)}^2 = \int_D e_{\text{ms}, \Delta}^{n+1} w_0 \, dx.$$

Consequently, an application of the Young's inequality implies

$$\left\| e_{\text{ms}, \Delta}^{n+1} \right\|_{L^2(D)} \leq \frac{1}{T^n T^{n+1}} (\Delta T)^2 \|v_1 - v_2\|_{L^2(D)}.$$

Analogously, we can obtain the estimate for $e_{\text{ms}, \delta}^{n+1}$, which reads

$$\left\| e_{\text{ms}, \delta}^{n+1} \right\|_{L^2(D)} \leq \frac{1}{T^n T^{n+1}} \delta t \Delta T \|v_1 - v_2\|_{L^2(D)}.$$

Note that $\delta t \ll \Delta T$, then a combination of the two estimates above with the triangle inequality, shows the second assertion. \square

Remark 5.1. Lemma 5.1 indicates that the approximation property of the jump operator $\mathcal{S}(T^n, \cdot)$ deteriorates when T^n is small.

We present in the next theorem the convergence rate of Algorithm 2 to Problems (1.1) in pointwise-in-time in $L^2(D)$ -norm. To derive it, we first decompose the error from Algorithm 2 as a summation of the error from WEMsFEM and the error from parareal algorithm. Then we estimate the former by energy method using argument analogous to [31, Theorem 1.5], and the latter can be estimated in a similar manner as in [16, Theorem 1].

Theorem 5.1 (Error estimate of Algorithm 2 to Problem (1.1) in $L^2(D)$ -norm). *Let Assumption 2.1 hold. Assume that the source term $f \in L^2([0, T]; \dot{H}^2(D))$ satisfying $\partial_t f \in L^2([0, T]; L^2(D))$ and initial data $u_0 \in \dot{H}^3(D) \cap H_0^1(D)$. Let $\ell \in \mathbb{N}_+$ be the level parameter. The coarse time step size and fine time step size are ΔT and δt . Let $u(\cdot, t) \in V$ be the solution to Problem (1.1) and let U_k^n be the solution from Algorithm 2 with iteration $k \in \mathbb{N}_+$. There holds*

$$\begin{aligned} \|u(\cdot, T^n) - U_k^n\|_{L^2(D)} &\lesssim (H + 2^{-\ell/2} \|\kappa\|_{L^\infty(\mathcal{F}_H)}) H |u_0|_2 + \delta t \left(|u_0|_3 + \|f\|_{L^2(I; \dot{H}^2(D))} + \|\partial_t f\|_{L^2(I; L^2(D))} \right) \\ &\quad + \left(\frac{1}{T^{n-1}} \right)^{k+1} \frac{1}{k!} (\Delta T)^{k+1} \|u_0\|_{L^2(D)}. \end{aligned} \quad (5.2)$$

Proof. We first define the multiscale solution to Problem (1.1) using Algorithm 1. Find $u_{\text{ms}, \ell}^{\text{EW}, m} \in V_{\text{ms}, \ell}^{\text{EW}}$ for $m = 1, \dots, M_\delta$, satisfying

$$\begin{aligned} \forall w_{\text{ms}} \in V_{\text{ms}, \ell}^{\text{EW}} : \left(\frac{u_{\text{ms}, \ell}^{\text{EW}, m} - u_{\text{ms}, \ell}^{\text{EW}, m-1}}{\delta t}, w_{\text{ms}} \right)_D + a(u_{\text{ms}, \ell}^{\text{EW}, m}, w_{\text{ms}}) &= (f(\cdot, t_m), w_{\text{ms}})_D \\ u_{\text{ms}, \ell}^{\text{EW}, 0} &= \mathcal{P}_\ell(u_0). \end{aligned} \quad (5.3)$$

Then we only need to estimate $\|u(\cdot, T^n) - u_{\text{ms}, \ell}^{\text{EW}, m}\|_{L^2(D)}$ and $\|u_{\text{ms}, \ell}^{\text{EW}, m} - U_k^n\|_{L^2(D)}$ for $m := \Delta T / \delta t \times n$. Note that $T^n = t_m$. Therefore, we can replace T^n with t_m . Similarly, let $m' := \Delta T / \delta t \times (n-1)$, then it holds $t_{m'} = T^{n-1}$.

Step 1. To estimate the first term $\|u(\cdot, t_m) - u_{\text{ms}, \ell}^{\text{EW}, m}\|_{L^2(D)}$, let $e_{\text{ms}}^m := u(\cdot, t_m) - u_{\text{ms}, \ell}^{\text{EW}, m}$, then for all $j \geq 1$ it holds

$$\begin{aligned} \forall w_{\text{ms}} \in V_{\text{ms}, \ell}^{\text{EW}} : \int_D (e_{\text{ms}}^j - e_{\text{ms}}^{j-1}) w_{\text{ms}} \, dx + \delta t \int_D \kappa \nabla e_{\text{ms}}^j \cdot \nabla w_{\text{ms}} \, dx &= \int_D w^j \cdot w_{\text{ms}} \, dx \\ e_{\text{ms}}^0 &= u_0 - \mathcal{P}_\ell(u_0) \end{aligned}$$

with

$$w^j = u(\cdot, t_j) - u(\cdot, t_{j-1}) - \delta t \times \partial_t u(\cdot, t_j).$$

Subsequently, similar proof to [31, Theorem 1.5] leads to

$$\begin{aligned} \|e_{\text{ms}}^m\|_{L^2(D)} + \delta t \|e_{\text{ms}}^m\|_{H_k^1(D)} &\lesssim \|e_{\text{ms}}^0\|_{L^2(D)} + \delta t \int_0^T \|\partial_{ss} u\|_{L^2(D)} \, ds \\ &\lesssim (H + 2^{-\ell/2} \|\kappa\|_{L^\infty(\mathcal{F}_H)}) H |u_0|_2 + \delta t \int_0^T \|\partial_{ss} u\|_{L^2(D)} \, ds \\ &\lesssim (H + 2^{-\ell/2} \|\kappa\|_{L^\infty(\mathcal{F}_H)}) H |u_0|_2 + \delta t \left(|u_0|_3 + \|f\|_{L^2(I; \dot{H}^2(D))} + \|\partial_t f\|_{L^2(I; L^2(D))} \right). \end{aligned} \quad (5.4)$$

Here, we have applied estimates (3.7), (2.2) and (2.3) in the last inequality.

Step 2. We estimate the error induced by parareal algorithm in the multiscale method, i.e., the second term $\|u_{\text{ms},\ell}^{\text{EW},m} - U_k^n\|_{L^2(D)}$. We will prove:

$$\|u_{\text{ms},\ell}^{\text{EW},m} - U_k^n\|_{L^2(D)} \lesssim \left(\frac{1}{T^{n-1}}\right)^{k+1} \frac{1}{k!} (\Delta T)^{k+1} \|u_0\|_{L^2(D)}. \quad (5.5)$$

We can obtain from Algorithm 2:

$$u_{\text{ms},\ell}^{\text{EW},m} - U_{k+1}^n = \mathcal{S}(T^{n-1}, u_{\text{ms},\ell}^{\text{EW},m'}) - \mathcal{S}(T^{n-1}, U_k^{n-1}) + E_{\Delta}^{\text{ms},\ell}(T^{n-1}, u_{\text{ms},\ell}^{\text{EW},m'}) - E_{\Delta}^{\text{ms},\ell}(T^{n-1}, U_{k+1}^{n-1}).$$

Consequently, an application of Lemma 5.1 leads to

$$\begin{aligned} & \|u_{\text{ms},\ell}^{\text{EW},m} - U_{k+1}^n\|_{L^2(D)} \\ & \leq \|\mathcal{S}(T^{n-1}, u_{\text{ms},\ell}^{\text{EW},m'}) - \mathcal{S}(T^{n-1}, U_k^{n-1})\|_{L^2(D)} + \|E_{\Delta}^{\text{ms},\ell}(T^{n-1}, u_{\text{ms},\ell}^{\text{EW},m'}) - E_{\Delta}^{\text{ms},\ell}(T^{n-1}, U_{k+1}^{n-1})\|_{L^2(D)} \\ & \lesssim \Delta T \int_{T^{n-1}}^{T^n} \|\partial_{ss} \bar{\mathcal{F}}^{\text{ms},\ell}(T^{n-1}, \Delta T, u_{\text{ms},\ell}^{\text{EW},m'} - U_k^{n-1})\|_{L^2(D)} ds + \|u_{\text{ms},\ell}^{\text{EW},m'} - U_{k+1}^{n-1}\|_{L^2(D)} \\ & \lesssim \frac{1}{T^{n-1}T^n} (\Delta T)^2 \|u_{\text{ms},\ell}^{\text{EW},m'} - U_k^{n-1}\|_{L^2(D)} + \|u_{\text{ms},\ell}^{\text{EW},m'} - U_{k+1}^{n-1}\|_{L^2(D)}. \end{aligned}$$

Whereas similar trick as in the proof of [16, Theorem 1] can be utilized here to prove estimate (5.5). Then a combination with (5.4) results in the desired estimate. \square

Note that Theorem 5.1 indicates that the Error estimate for Algorithm 2 to Problems (1.1) in $L^2(D)$ -norm will deteriorate when the time step approaches the original $t = 0$. This blow-up of error is produced by the parareal algorithm (Step 2 in the proof to Theorem 5.1), which essentially arises from the approximation property of the jump operator (5.1). This estimate can be improved to

$$\|\mathcal{S}(T^n, v_1) - \mathcal{S}(T^n, v_2)\|_{L^2(D)} \leq (\Delta T)^2 |v_1 - v_2|_4, \quad (5.6)$$

when $v_1, v_2 \in \dot{H}_4(D)$.

However, the estimate above has different norms on both sides of the inequality. This makes the argument in Step 2, proof to Theorem 5.1 invalid.

When iteration $k = 0$, an application to Step 1, proof to Theorem 5.1 results in

$$\|u(\cdot, T^n) - U_0^n\|_{L^2(D)} \lesssim (H + 2^{-\ell/2} \|\kappa\|_{L^\infty(\mathcal{F}_H)}) H |u_0|_2 + \Delta t \left(|u_0|_3 + \|f\|_{L^2(I; \dot{H}^2(D))} + \|\partial_t f\|_{L^2(I; L^2(D))} \right).$$

Remark 5.2. Algorithm 2 outweighs Algorithm 1 only when the former achieves similar accuracy to the latter within a very few iteration $k \ll M_\Delta$. Therefore, we are not interested in the case when $k \geq M_\Delta$ or the error at time level T^n with $k \geq n$.

6 Numerical Results

In this section, we perform a series of numerical experiments to demonstrate the performance of the proposed WEMP Algorithm, i.e. Algorithm 2.

We consider the parabolic equation (1.1) in the space domain $D := [0, 1]^2$ and the time domain $[0, T] = [0, 1]$. The permeability coefficient κ is depicted in Figure 2 (left figure), which is high-contrast and heterogenous. The smooth initial data tested in our numerical experiments is chosen to be $u_0 := x(1-x)y(1-y)$. We refer to Figure 2 (right figure) for an illustration.

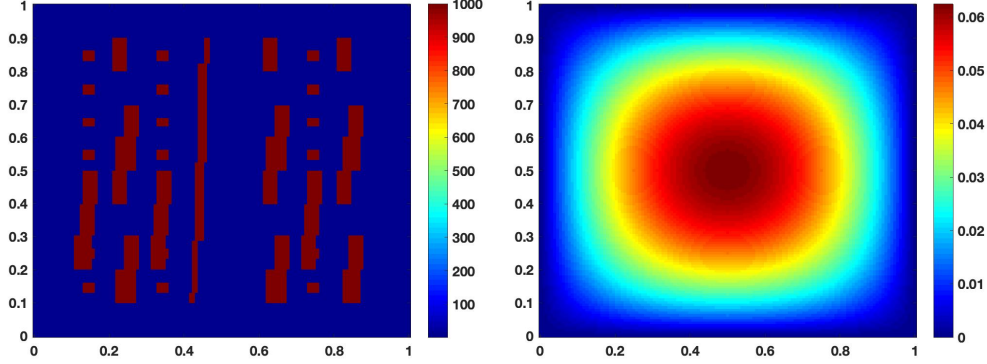


Figure 2: The heterogeneous permeability field κ and the initial data $u_0 = x(1-x)y(1-y)$.

Let \mathcal{T}_H be a decomposition of the domain D into non-overlapping shape-regular rectangular elements with maximal mesh size $H := 2^{-4}$. These coarse rectangular elements are further partitioned into a collection of connected fine rectangular elements \mathcal{T}_h using fine mesh size $h := 2^{-7}$. Similarly, we define V_h to be a conforming piecewise affine finite element associated with \mathcal{T}_h . In our numerical experiments, space meshes \mathcal{T}_H and \mathcal{T}_h are fixed. To keep our presentation concise, we will only present the numerical results with a fixed level parameter $\ell := 2$. The temporal discretization is presented in Section 2 with $T := 1$. The coarse time step size and fine time step size are ΔT and δt . Note that $\delta t \ll \Delta T$.

We introduce the following notations to calculate the errors. The relative errors for the multiscale solution in $L^2(D)$ -norm and $H_\kappa^1(D)$ -norm are

$$\text{Rel}_{L^2}^{\text{EW}}(T^n) := \frac{\|u_h^n - u_{\text{ms},\ell}^{\text{EW},n}\|_{L^2(D)}}{\|u_h^n\|_{L^2(D)}} \times 100 \quad \text{and} \quad \text{Rel}_{H_\kappa^1}^{\text{EW}}(T^n) := \frac{\|u_h^n - u_{\text{ms},\ell}^{\text{EW},n}\|_{H_\kappa^1(D)}}{\|u_h^n\|_{H_\kappa^1(D)}} \times 100.$$

Analogously, the relative errors for our proposed algorithm with iteration $k \in \mathbb{N}$ in $L^2(D)$ -norm and $H_\kappa^1(D)$ -norm are

$$\text{Rel}_{L^2}^k(T^n) := \frac{\|u_h^m - U_k^n\|_{L^2(D)}}{\|u_h^m\|_{L^2(D)}} \times 100 \quad \text{and} \quad \text{Rel}_{H_\kappa^1}^k(T^n) := \frac{\|u_h^m - U_k^n\|_{H_\kappa^1(D)}}{\|u_h^m\|_{H_\kappa^1(D)}} \times 100$$

with $m := \Delta T / \delta t \times n$.

Our numerical experiments include testing nonzero source term in section 6.1 and zero source term in section 6.2. We test what differences backward Euler Galerkin Method and Crank-Nicolson Galerkin Method will make to the error. We also study how fine solver and coarse solver will influence the error and iteration number.

6.1 Numerical tests with nonzero source term

To define nonzero source term, we take time-dependent smooth function

$$f(x, y, t) := 200\pi^2 \sin(\pi x) \sin(\pi y) \sin(10\pi t x).$$

Since there is no analytic solution to system (1.1), we need to find an approximation of the exact solutions. To this end, we take time step size $\delta t = 10^{-4}$ and use backward Euler Galerkin Method in (2.4) to obtain the reference solutions u_h^n . Note that we use a much finer time step size to simulate the reference solution. We plot the reference solutions u_h^n for $n = 10^3, 3 \times 10^3, 5 \times 10^3$ and 10^4 in Figure 3.

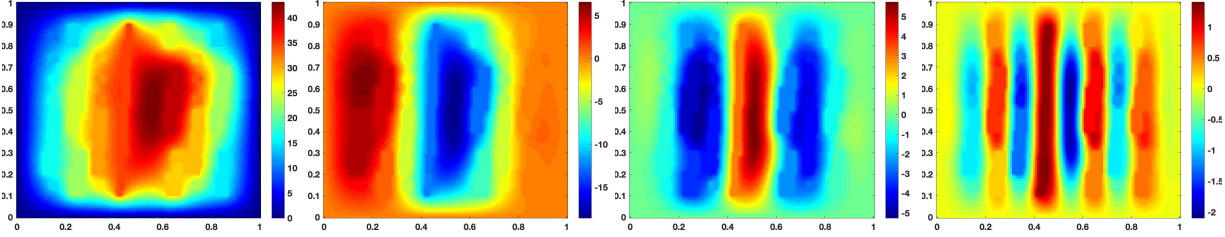


Figure 3: Numerical solution u_h^n to (2.4) for $n = 10^3, 3 \times 10^3, 5 \times 10^3$ and 10^4 with $\delta t = 10^{-4}$.

In the rest of this subsection, we will present numerical tests using backward Euler scheme with $\frac{\Delta T}{\delta t} = 100$ in Experiment 1, Crank-Nicolson scheme with $\frac{\Delta T}{\delta t} = 100$ in Experiment 2 and backward Euler scheme with $\frac{\Delta T}{\delta t} = 10$ in Experiment 3. For all the three experiments, our proposed algorithm, i.e. Algorithm 2, can generate numerical solutions by a few iterations at least of the same accuracy as the multiscale solutions from Algorithm 1.

Experiment 1: Backward Euler with $\frac{\Delta T}{\delta t} = 100$

We test in this experiment the performance of Algorithm 2 with a fine time step $\delta t = 10^{-3}$ and a coarse time step $\Delta T = 0.1$. The backward Euler scheme is utilized for the time discretization.

The multiscale solutions $u_{ms,\ell}^{EW,m}$ for $m = 100, 300, 500, 1000$ from Algorithm 1 are presented in Figure 4. In comparison, we present the numerical solutions U_k^n for $n = 1, 3, 5, 10$ from Algorithm 2 with iteration number $k = 0, 1$ and 2 in Figure 5. One can observe that U_k^n converges to the multiscale solution $u_{ms,\ell}^{EW,n}$ as the iteration k increases.

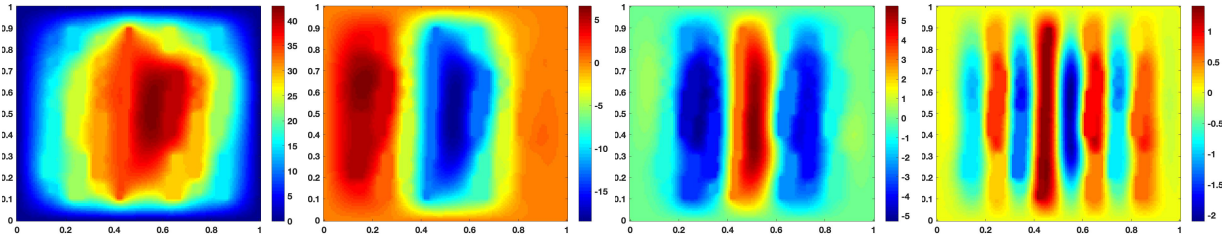


Figure 4: Multiscale solution from Algorithm 1 with $\delta t = 10^{-3}$ and $\ell = 2$, backward Euler scheme: $u_{ms,\ell}^{EW,100}$, $u_{ms,\ell}^{EW,300}$, $u_{ms,\ell}^{EW,500}$ and $u_{ms,\ell}^{EW,1000}$.

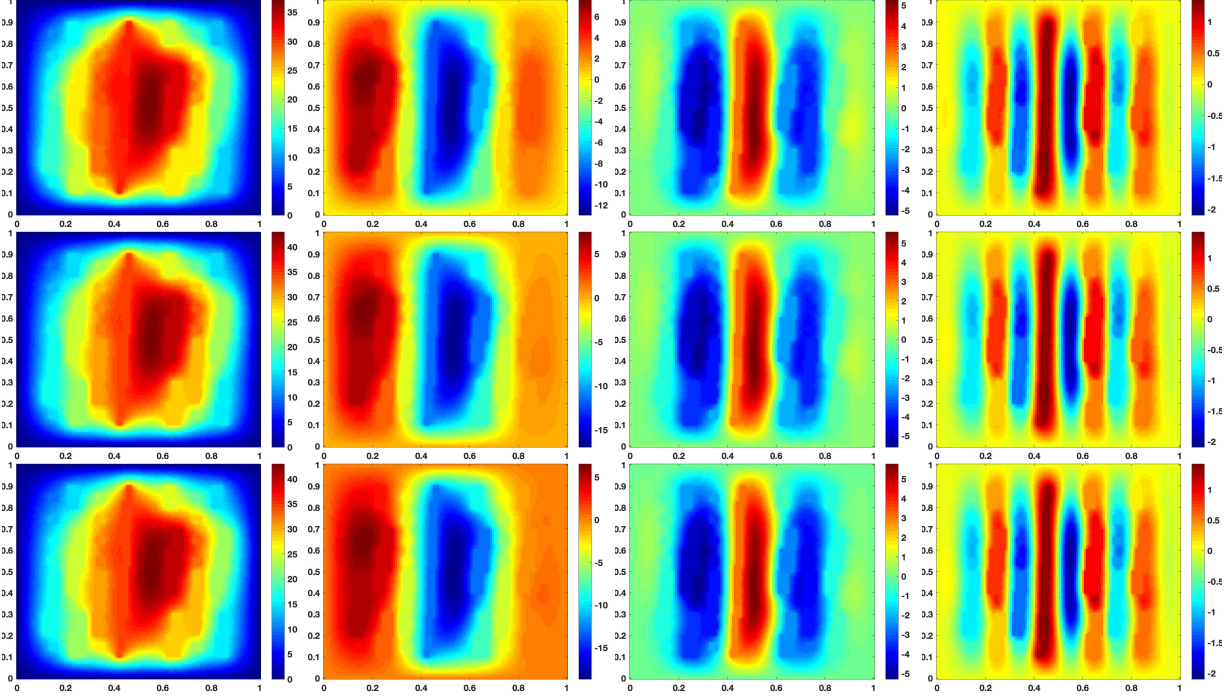


Figure 5: Numerical solutions U_k^n for $n = 1, 3, 5, 10$ from Algorithm 2 with $\Delta T = 0.1$ and $\delta t = 10^{-3}$, backward Euler scheme: iteration number $k = 0$ (top), $k = 1$ (middle) and $k = 2$ (bottom).

We present the convergence history of Algorithm 2 in relative $L^2(D)$ error and relative $H^1_\kappa(D)$ error in Tables 1 and 2. In each table, the second column displays the relative error between numerical solutions $u_{ms,\ell}^{EW,n}$ from Algorithm 1 and reference solutions u_h^n . The relative errors between numerical solutions U_k^n from Algorithm 2 and reference solutions u_h^n are displayed from the third column towards the last column.

T^n	$\text{Rel}_{L^2}^{EW}(T^n)$	$\text{Rel}_{L^2}^0(T^n)$	$\text{Rel}_{L^2}^1(T^n)$	$\text{Rel}_{L^2}^2(T^n)$	$\text{Rel}_{L^2}^3(T^n)$	$\text{Rel}_{L^2}^4(T^n)$
0.1	0.5671	14.3828	0.5671	0.5671	0.5671	0.5671
0.2	0.8234	30.6711	4.0891	0.8234	0.8234	0.8234
0.3	0.8258	42.2133	13.6117	0.9514	0.8258	0.8258
0.4	0.5897	22.5947	8.2614	4.9882	0.5569	0.5897
0.5	0.5323	11.4592	6.4804	1.1830	2.2190	0.5022
0.6	0.7072	8.6259	1.8506	2.0906	1.1444	0.7087
0.7	0.7229	8.9372	1.0193	1.2827	0.7229	0.7531
0.8	0.9680	11.0146	1.9673	0.9901	1.0137	0.9766
0.9	1.0681	6.2513	1.9613	1.2086	1.0517	1.0779
1.0	0.9145	5.1982	1.0812	0.9423	0.9399	0.9096

Table 1: Convergence history of Algorithm 2 in relative $L^2(D)$ error for Experiment 1: backward Euler scheme with $\Delta T = 0.1$ and $\delta t = 10^{-3}$.

T^n	$\text{Rel}_{H_\kappa^1}^{\text{EW}}(T^n)$	$\text{Rel}_{H_\kappa^1}^0(T^n)$	$\text{Rel}_{H_\kappa^1}^1(T^n)$	$\text{Rel}_{H_\kappa^1}^2(T^n)$	$\text{Rel}_{H_\kappa^1}^3(T^n)$	$\text{Rel}_{H_\kappa^1}^4(T^n)$
0.1	6.9437	16.5638	6.9437	6.9437	6.9437	6.9437
0.2	5.6489	25.0878	6.6353	5.6489	5.6489	5.6489
0.3	4.9158	27.6524	9.5624	4.9600	4.9158	4.9158
0.4	4.7240	16.6013	6.2652	5.2435	4.7283	4.7240
0.5	4.8984	9.3734	5.6879	4.9166	4.9356	4.8997
0.6	5.3109	7.9758	5.3640	5.3383	5.3148	5.3130
0.7	5.3064	6.9107	5.3173	5.3128	5.3066	5.3067
0.8	6.2666	7.6015	6.2857	6.2666	6.2671	6.2667
0.9	6.4270	7.0167	6.4435	6.4279	6.4270	6.4270
1.0	4.9341	5.2526	4.9371	4.9343	4.9341	4.9341

Table 2: Convergence history of Algorithm 2 in relative $H_\kappa^1(D)$ error for Experiment 1: backward Euler scheme with $\Delta T = 0.1$ and $\delta t = 10^{-3}$.

One can observe from Tables 1 and 2 that 4 iterations is sufficient for Algorithm 2 to attain the same accuracy as Algorithm 1 for all discrete time levels under the $L^2(D)$ -norm, while 2 iterations under $H_\kappa^1(D)$ -norm. For each iteration, it involves solving the original system for 10 times using coarse solver and using fine solvers for 100 times on each time interval in parallel. However, to obtain multiscale solutions from Algorithm 1, it involves solving original system for about 1000 times. So, with the aid of large number of processors, it could save a lot of time to obtain numerical solutions from Algorithm 2.

Experiment 2: Crank-Nicolson with $\frac{\Delta T}{\delta t} = 100$

Since the backward Euler scheme is only first order accurate, a higher order accurate scheme can improve the performance of Algorithm 1 and Algorithm 2. This can be seen from the proof to Theorem 5.1. In this section, we will present the numerical tests with Crank-Nicolson scheme for both algorithms.

A direct application of Crank-Nicolson scheme as a time discretization fails to maintain second order accuracy due to the possible blow up of the eigenvalues of the elliptic operator $-\nabla \cdot (\kappa \nabla \cdot)$ when $\eta_{\max} \rightarrow \infty$. To improve its performance and maintain second order convergence rate, we use 3 steps of backward Euler scheme before Crank-Nicolson scheme kicks in [26, 31].

The multiscale solutions from Algorithm 1 with Crank-Nicolson scheme are presented in Figure 6. We present the numerical solutions U_k^n for $n = 1, 3, 5, 10$ from Algorithm 2 with iteration $k = 0, 1, 2$ in Figure 7. One can observe the same convergence behavior as in Experiment 1.

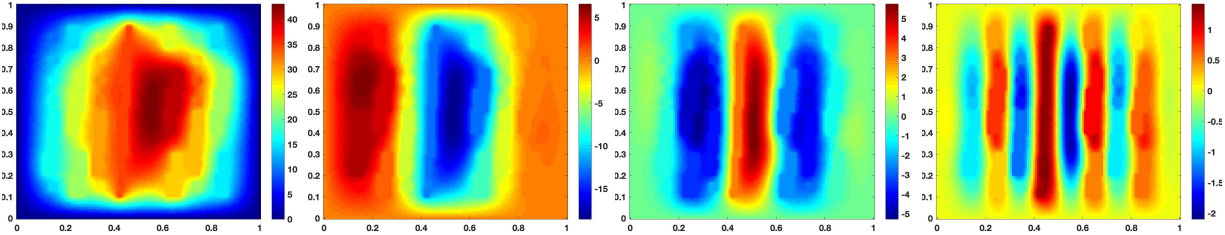


Figure 6: Multiscale solution from Algorithm 1 with $\delta t = 10^{-3}$ and $\ell = 2$, Crank-Nicolson scheme: $u_{\text{ms},\ell}^{\text{EW},100}$, $u_{\text{ms},\ell}^{\text{EW},300}$, $u_{\text{ms},\ell}^{\text{EW},500}$ and $u_{\text{ms},\ell}^{\text{EW},1000}$.

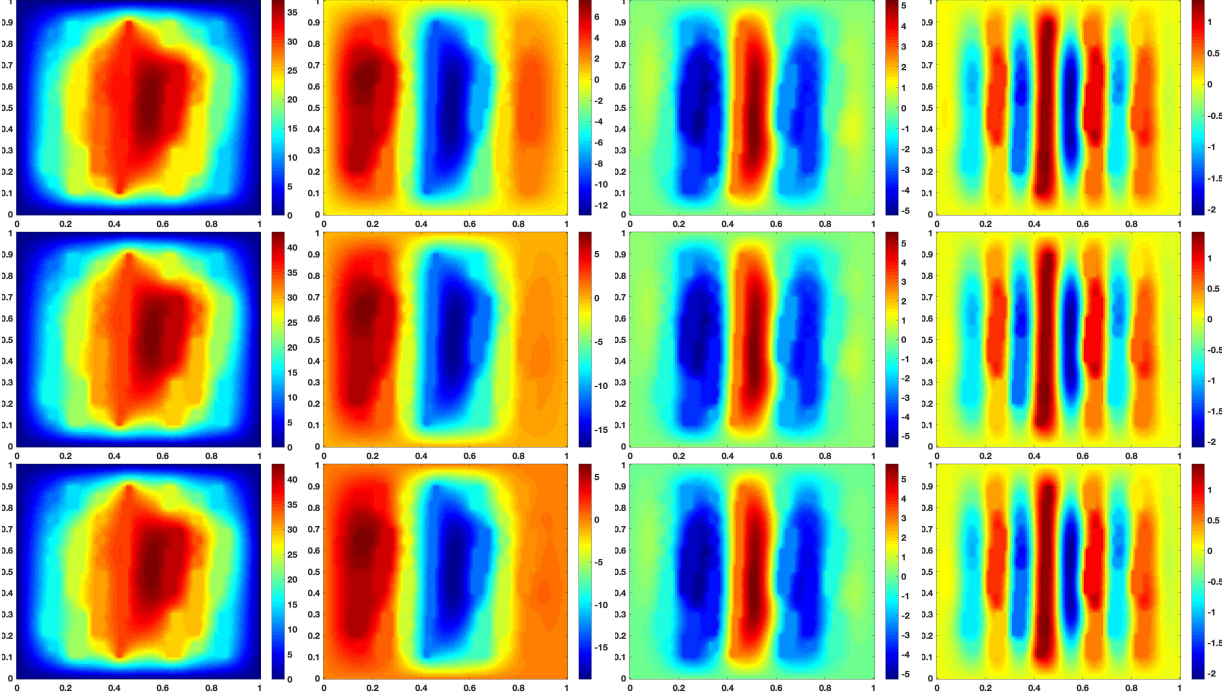


Figure 7: Numerical solutions U_k^n for $n = 1, 3, 5, 10$ from Algorithm 2 with $\Delta T = 0.1$ and $\delta t = 10^{-3}$, Crank-Nicolson scheme: iteration number $k = 0$ (top), $k = 1$ (middle) and $k = 2$ (bottom).

The convergence history of Algorithm 2 in $L^2(D)$ -norm and $H_\kappa^1(D)$ -norm is presented in Tables 3 and 4, respectively. Similar to Experiment 1, we observe that 4 iterations is sufficient for Algorithm 2 to reach the same accuracy as Algorithm 1 at all discrete time levels under the $L^2(D)$ -norm, while 2 iterations under the $H_\kappa^1(D)$ -norm. Comparing Table 1 with Table 3, one observes that Algorithm 2 with Crank-Nicolson scheme outperforms that with backward Euler scheme under $L^2(D)$ -norm.

T^n	$\text{Rel}_{L^2}^{\text{EW}}(T^n)$	$\text{Rel}_{L^2}^0(T^n)$	$\text{Rel}_{L^2}^1(T^n)$	$\text{Rel}_{L^2}^2(T^n)$	$\text{Rel}_{L^2}^3(T^n)$	$\text{Rel}_{L^2}^4(T^n)$
0.1	0.3527	14.3828	0.3527	0.3527	0.3527	0.3527
0.2	0.5438	30.6711	4.3959	0.5485	0.5485	0.5485
0.3	0.3510	42.2133	13.2555	1.6259	0.3515	0.3515
0.4	0.3443	22.5947	8.2409	4.9804	0.5513	0.3431
0.5	0.4847	11.4592	6.4455	1.0726	2.2873	0.4642
0.6	0.7121	8.6259	1.7874	2.1688	1.1929	0.6720
0.7	0.7049	8.9372	0.9898	1.2377	0.7162	0.7834
0.8	0.9467	11.0146	1.8508	0.9946	0.9773	0.9465
0.9	1.0636	6.2513	1.8811	1.1818	1.0505	1.0737
1.0	0.9072	5.1982	1.0806	0.9286	0.9252	0.9054

Table 3: Convergence history of Algorithm 2 in relative $L^2(D)$ error for Experiment 2: Crank-Nicolson scheme with $\Delta T = 0.1$ and $\delta t = 10^{-3}$.

T^n	$\text{Rel}_{H_\kappa^1}^{\text{EW}}(T^n)$	$\text{Rel}_{H_\kappa^1}^0(T^n)$	$\text{Rel}_{H_\kappa^1}^1(T^n)$	$\text{Rel}_{H_\kappa^1}^2(T^n)$	$\text{Rel}_{H_\kappa^1}^3(T^n)$	$\text{Rel}_{H_\kappa^1}^4(T^n)$
0.1	6.9448	16.5638	6.9448	6.9448	6.9448	6.9448
0.2	5.6381	25.0878	6.7485	5.6383	5.6383	5.6383
0.3	4.9062	27.6524	9.3773	5.0384	4.9062	4.9062
0.4	4.7218	16.6013	6.2318	5.2453	4.7328	4.7218
0.5	4.8979	9.3734	5.6700	4.9104	4.9386	4.8996
0.6	5.3108	7.9758	5.3592	5.3401	5.3153	5.3126
0.7	5.3062	6.9107	5.3156	5.3121	5.3064	5.3069
0.8	6.2664	7.6015	6.2824	6.2667	6.2669	6.2664
0.9	6.4269	7.0167	6.4412	6.4274	6.4270	6.4269
1.0	4.9341	5.2526	4.9369	4.9343	4.9340	4.9341

Table 4: Convergence history of Algorithm 2 in relative $H_\kappa^1(D)$ error for Experiment 2: Crank-Nicolson scheme with $\Delta T = 0.1$ and $\delta t = 10^{-3}$.

Experiment 3: backward Euler with $\frac{\Delta T}{\delta t} = 10$

We are also interested in studying how the coarse solver and fine solver affect the performance of our proposed WEMP algorithm. To this end, we choose $\Delta T = 10^{-2}$, $\delta t = 10^{-3}$ and utilize backward Euler scheme in time discretization. Note that the ratio between the coarse time step and fine time step is smaller than that in Experiment 1.

The multiscale solutions from Algorithm 1 with backward Euler scheme are presented in Figure 8. We present the numerical solutions U_k^n for $n = 10, 30, 50, 100$ from Algorithm 2 with iteration number $k = 0, 1, 2$ in Figure 9. One can observe the same convergence behavior as in Experiment 1.

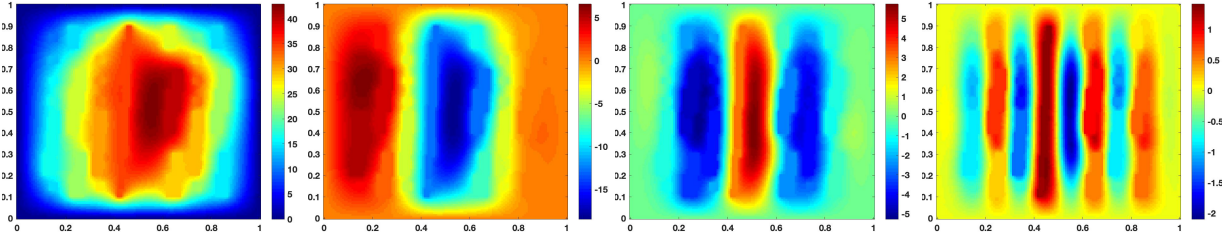


Figure 8: Multiscale solution from Algorithm 1 with $\delta t = 10^{-3}$ and $\ell = 2$, backward Euler scheme: $u_{\text{ms},\ell}^{\text{EW},100}$, $u_{\text{ms},\ell}^{\text{EW},300}$, $u_{\text{ms},\ell}^{\text{EW},500}$ and $u_{\text{ms},\ell}^{\text{EW},1000}$.

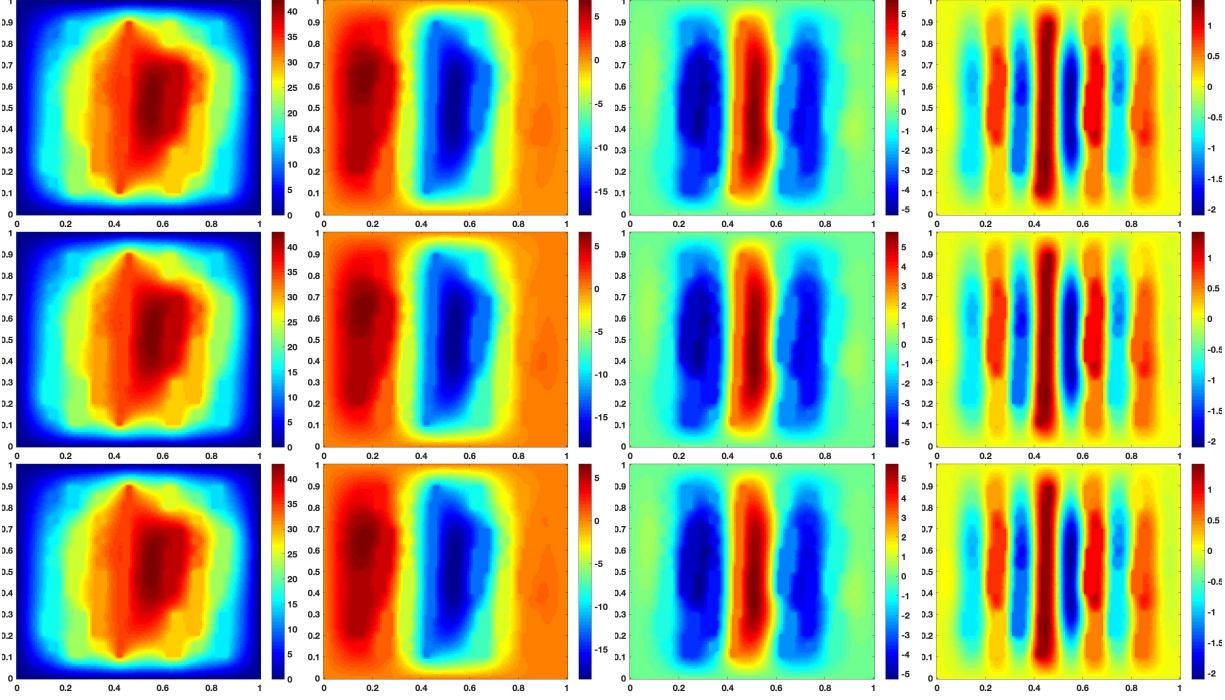


Figure 9: Numerical solutions U_k^n for $n = 10, 30, 50, 100$ from Algorithm 2 with $\Delta T = 10^{-2}$ and $\delta t = 10^{-3}$, backward Euler scheme: iteration $k = 0$ (top), $k = 1$ (middle) and $k = 2$ (bottom).

The convergence history of Algorithm 2 in $L^2(D)$ -norm and $H_\kappa^1(D)$ -norm is presented in Tables 5 and 6. Comparing Table 1 with Table 5, one can see 1 iteration is sufficient for the numerical solutions from Algorithm 2 to reach the same accuracy as multiscale solutions from Algorithm 1 under $L^2(D)$ -norm and $H_\kappa^1(D)$ -norm when the coarse time step $\Delta T = 10^{-2}$ becomes smaller. However, this involves more coarse solvers for each iteration. Furthermore, a decreased coarse time step is only practical when sufficient processors are available.

T^n	$\text{Rel}_{L^2}^{\text{EW}}(T^n)$	$\text{Rel}_{L^2}^0(T^n)$	$\text{Rel}_{L^2}^1(T^n)$	$\text{Rel}_{L^2}^2(T^n)$	$\text{Rel}_{L^2}^3(T^n)$	$\text{Rel}_{L^2}^4(T^n)$
0.1	0.5671	2.4095	0.6072	0.5563	0.5680	0.5670
0.2	0.8234	3.4560	0.4291	0.8527	0.8237	0.8230
0.3	0.8258	6.2194	0.4501	0.8474	0.8253	0.8258
0.4	0.5897	3.0769	0.5520	0.6288	0.5874	0.5891
0.5	0.5323	1.9183	0.5216	0.5621	0.5273	0.5332
0.6	0.7072	1.1525	0.6757	0.7204	0.7052	0.7078
0.7	0.7229	1.4333	0.7154	0.7287	0.7222	0.7229
0.8	0.9680	1.9263	0.9493	0.9720	0.9680	0.9679
0.9	1.0681	1.6490	1.0817	1.0673	1.0684	1.0681
1.0	0.9145	1.1618	0.9204	0.9146	0.9145	0.9146

Table 5: Convergence history of Algorithm 2 in relative $L^2(D)$ error for Experiment 3: backward Euler scheme with $\Delta T = 10^{-2}$ and $\delta t = 10^{-3}$.

T^n	$\text{Rel}_{H_\kappa^1}^{\text{EW}}(T^n)$	$\text{Rel}_{H_\kappa^1}^0(T^n)$	$\text{Rel}_{H_\kappa^1}^1(T^n)$	$\text{Rel}_{H_\kappa^1}^2(T^n)$	$\text{Rel}_{H_\kappa^1}^3(T^n)$	$\text{Rel}_{H_\kappa^1}^4(T^n)$
0.1	6.9437	7.2482	6.9435	6.9438	6.9437	6.9437
0.2	5.6489	6.2363	5.6351	5.6509	5.6488	5.6489
0.3	4.9158	6.1653	4.9083	4.9177	4.9157	4.9158
0.4	4.7240	5.0851	4.7270	4.7260	4.7239	4.7240
0.5	4.8984	5.0041	4.8988	4.8993	4.8984	4.8984
0.6	5.3109	5.3409	5.3116	5.3114	5.3108	5.3109
0.7	5.3064	5.3324	5.3066	5.3066	5.3064	5.3064
0.8	6.2666	6.2916	6.2667	6.2667	6.2666	6.2666
0.9	6.4270	6.4420	6.4270	6.4270	6.4270	6.4270
1.0	4.9341	4.9390	4.9341	4.9341	4.9341	4.9341

Table 6: Convergence history of Algorithm 2 in relative $H_\kappa^1(D)$ error for Experiment 3: backward Euler scheme with $\Delta T = 10^{-2}$ and $\delta t = 10^{-3}$.

6.2 Numerical tests with zero source term

In this section, we test the performance of Algorithm 2 for Problem (1.1) with backward Euler scheme and Crank-Nicolson scheme. The source term $f := 0$. Consequently, the solution decays rapidly to 0. To generate solutions with reasonable size, we set the final time $T = 0.1$, the coarse time step $\Delta T := 10^{-2}$ and the fine time step $\delta t = 10^{-3}$. The initial data and permeability are the same as in the previous section. We use backward Euler scheme with time step 10^{-3} to solve for the reference solutions u_h^n . The reference solutions u_h^n for $n = 10, 30, 50, 100$ are plotted in Figure 10.

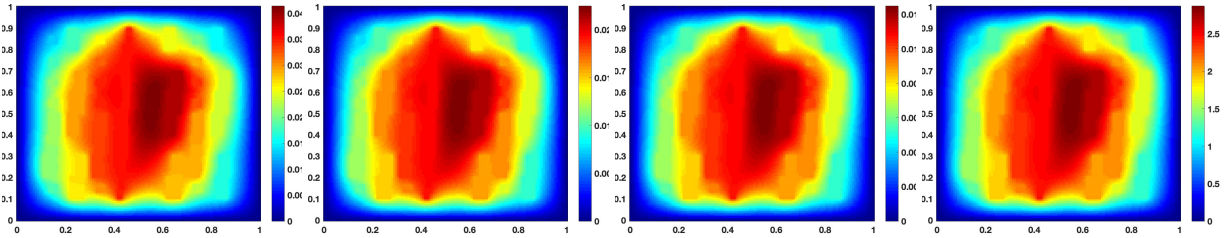


Figure 10: Numerical solutions u_h^n to (2.4) with $f = 0$ for $n = 10, 30, 50$ and 100 with $\delta t = 10^{-3}$.

The multiscale solutions $u_{\text{ms},\ell}^{\text{EW},n}$ for $n = 10, 30, 50, 100$ from Algorithm 1 with backward Euler scheme and time step size $\delta t = 10^{-3}$ are presented in Figure 11. We present the numerical solutions U_k^n for $n = 1, 3, 5, 10$ from Algorithm 2 with iteration number $k = 0, 1, 2$ in Figure 12. One can observe U_k^n converges to $u_{\text{ms},\ell}^{\text{EW},n}$ as the iteration number k increases.

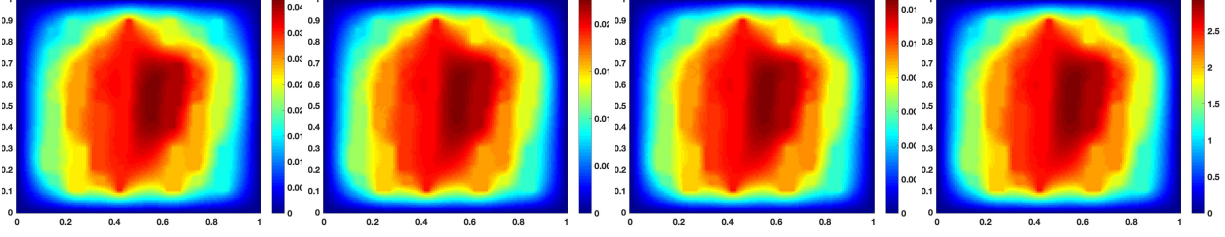


Figure 11: Multiscale solutions from Algorithm 1 with $\delta t = 10^{-3}$ and $\ell = 2$, backward Euler scheme: $u_{ms,\ell}^{EW,10}$, $u_{ms,\ell}^{EW,30}$, $u_{ms,\ell}^{EW,50}$ and $u_{ms,\ell}^{EW,100}$.

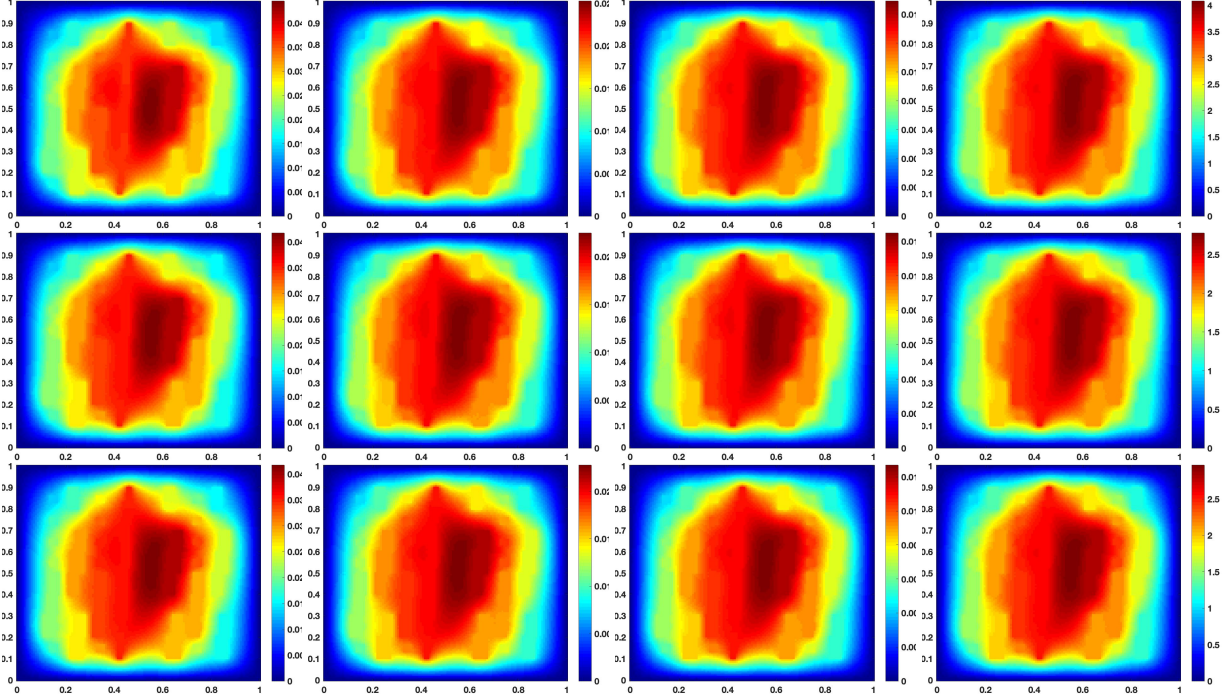


Figure 12: Numerical solutions U_k^n for $n = 1, 3, 5, 10$ from Algorithm 2 with $\Delta T = 10^{-2}$ and $\delta t = 10^{-3}$, backward Euler scheme: iteration number $k = 0$ (top), $k = 1$ (middle) and $k = 2$ (bottom).

The convergence history of Algorithm 2 in $L^2(D)$ -norm and $H^1_\kappa(D)$ -norm is presented in Tables 7 and 8. From the two tables, we see that 1 iteration is sufficient for the numerical solutions from Algorithm 2 with backward Euler to converge under $L^2(D)$ -norm and $H^1_\kappa(D)$ -norm. We can conclude that our proposed algorithm with backward Euler scheme is effective in solving Problem (1.1) with zero source term.

T^n	$\text{Rel}_{L^2}^{\text{EW}}(T^n)$	$\text{Rel}_{L^2}^0(T^n)$	$\text{Rel}_{L^2}^1(T^n)$	$\text{Rel}_{L^2}^2(T^n)$	$\text{Rel}_{L^2}^3(T^n)$	$\text{Rel}_{L^2}^4(T^n)$
0.01	0.4381	4.8988	0.4381	0.4381	0.4381	0.4381
0.02	0.5265	7.3857	0.7332	0.5265	0.5265	0.5265
0.03	0.7540	11.0428	0.7002	0.7764	0.7540	0.7540
0.04	0.9925	14.9558	0.5013	1.0253	0.9929	0.9925
0.05	1.2334	19.0240	0.2844	1.2816	1.2342	1.2334
0.06	1.4757	23.2389	0.3941	1.5582	1.4751	1.4758
0.07	1.7191	27.6036	0.8900	1.8610	1.7154	1.7192
0.08	1.9633	32.1231	1.5819	2.1943	1.9544	1.9636
0.09	2.2084	36.8028	2.4535	2.5635	2.1913	2.2090
0.10	2.4542	41.6483	3.5123	2.9751	2.4247	2.4554

Table 7: Convergence history of Algorithm 2 in relative $L^2(D)$ error for $f = 0$: backward Euler scheme with $\Delta T = 10^{-2}$ and $\delta t = 10^{-3}$.

T^n	$\text{Rel}_{H_\kappa^1}^{\text{EW}}(T^n)$	$\text{Rel}_{H_\kappa^1}^0(T^n)$	$\text{Rel}_{H_\kappa^1}^1(T^n)$	$\text{Rel}_{H_\kappa^1}^2(T^n)$	$\text{Rel}_{H_\kappa^1}^3(T^n)$	$\text{Rel}_{H_\kappa^1}^4(T^n)$
0.01	7.1035	14.3354	7.1035	7.1035	7.1035	7.1035
0.02	7.0711	11.3573	7.3430	7.0711	7.0711	7.0711
0.03	7.1069	13.6291	7.2438	7.1275	7.1069	7.1069
0.04	7.1544	17.0111	7.1216	7.1801	7.1551	7.1544
0.05	7.2098	20.7809	7.0502	7.2335	7.2115	7.2098
0.06	7.2727	24.7976	7.0138	7.3016	7.2741	7.2728
0.07	7.3432	29.0209	7.0171	7.3900	7.3432	7.3434
0.08	7.4211	33.4354	7.0887	7.5022	7.4188	7.4214
0.09	7.5064	38.0353	7.2745	7.6424	7.5006	7.5068
0.10	7.5990	42.8190	7.6303	7.8168	7.5877	7.5995

Table 8: Convergence history of Algorithm 2 in relative $H_\kappa^1(D)$ error for $f = 0$: backward Euler scheme with $\Delta T = 10^{-2}$ and $\delta t = 10^{-3}$.

Our last experiment is replacing backward Euler scheme by Crank-Nicolson scheme for the above problem. The corresponding multiscale solutions from Algorithm 1 are presented in Figure 13. We present the numerical solutions U_k^n from Algorithm 2 for $n = 1, 3, 5, 10$ with iteration number $k = 0, 2, 4$ in Figure 14.

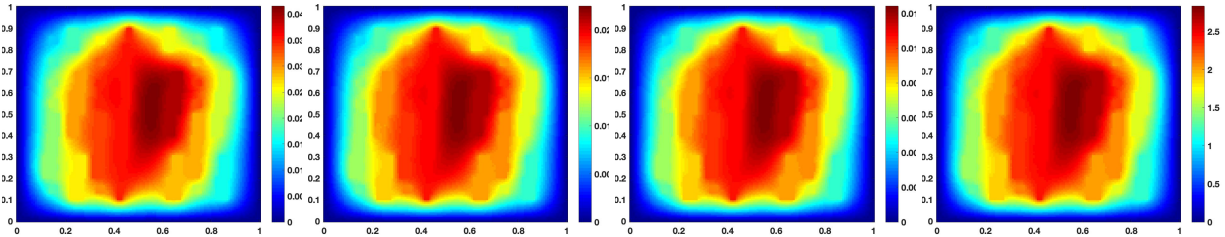


Figure 13: Multiscale solution from Algorithm 1 with $\delta t = 10^{-3}$ and $\ell = 2$, Crank-Nicolson scheme: $u_{\text{ms},\ell}^{\text{EW},10}$, $u_{\text{ms},\ell}^{\text{EW},30}$, $u_{\text{ms},\ell}^{\text{EW},50}$ and $u_{\text{ms},\ell}^{\text{EW},100}$.

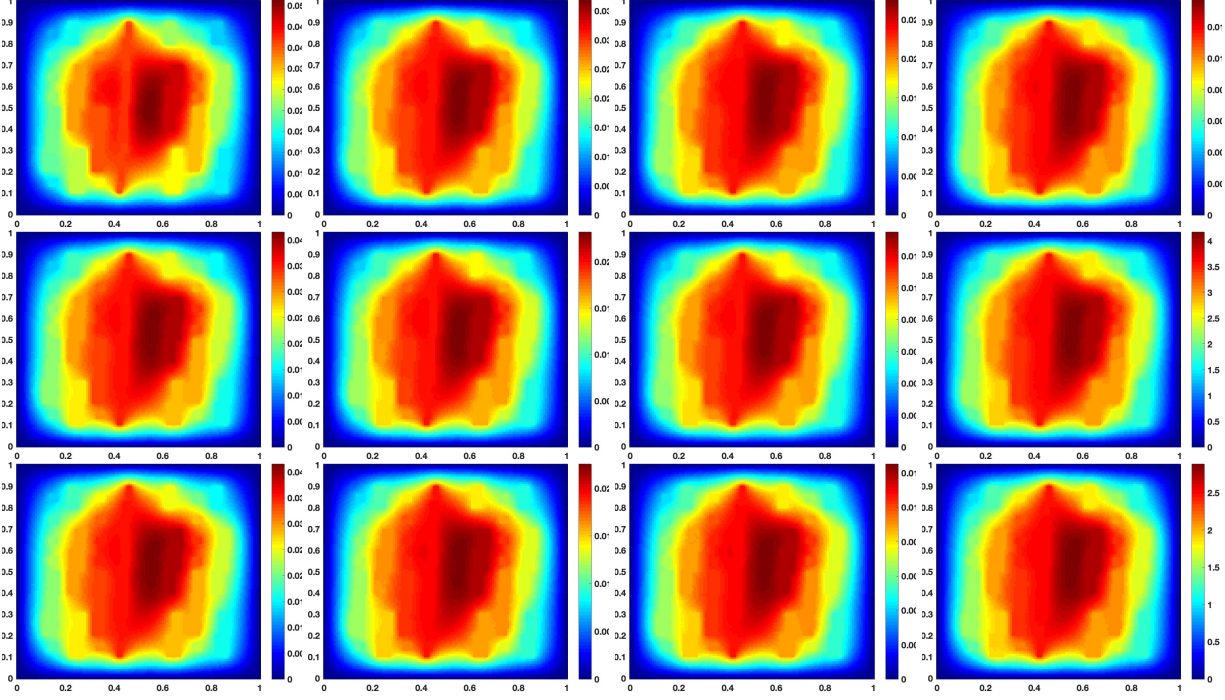


Figure 14: Numerical solutions U_k^n for $n = 1, 3, 5, 10$ from Algorithm 2 with $\Delta T = 10^{-2}$ and $\delta t = 10^{-3}$, Crank-Nicolson scheme: iteration number $k = 0$ (top), $k = 2$ (middle) and $k = 4$ (bottom).

The convergence history of Algorithm 2 in $L^2(D)$ -norm and $H_\kappa^1(D)$ -norm is presented in Tables 9 and 10. One observes that it takes 4 iterations to converge under $L^2(D)$ -norm and 3 iterations to converge under $H_\kappa^1(D)$ -norm when using Algorithm 2 with Crank-Nicolson scheme. Comparing Table 7 with Table 9, we can see that Algorithm 2 with the Crank-Nicolson scheme yields a better accuracy than that with the backward Euler scheme. We conclude that Algorithm 2 with backward Euler scheme converges faster than that with Crank-Nicolson scheme, while Algorithm 2 with Crank-Nicolson scheme generate solutions with a higher accuracy for Problem (1.1) with zero source term.

T^n	$\text{Rel}_{L^2}^{\text{EW}}(T^n)$	$\text{Rel}_{L^2}^0(T^n)$	$\text{Rel}_{L^2}^1(T^n)$	$\text{Rel}_{L^2}^2(T^n)$	$\text{Rel}_{L^2}^3(T^n)$	$\text{Rel}_{L^2}^4(T^n)$
0.01	0.1915	17.9465	13.3079	0.1677	0.1677	0.1677
0.02	0.2209	36.8558	29.6961	0.7619	0.1607	0.1607
0.03	0.3817	59.7687	50.4219	1.8702	0.2242	0.1687
0.04	0.5603	86.6988	75.8706	3.5561	0.3974	0.1805
0.05	0.7439	118.2106	106.8652	6.2307	0.5572	0.2087
0.06	0.9293	155.0529	144.3583	10.1676	0.7313	0.2443
0.07	1.1155	198.1194	189.4784	15.6176	1.0374	0.2676
0.08	1.3020	248.4594	243.5539	22.8847	1.5818	0.2717
0.09	1.4886	307.3003	308.1424	32.3420	2.4362	0.2607
0.10	1.6751	376.0776	385.0672	44.4367	3.6758	0.2492

Table 9: Convergence history of Algorithm 2 in relative $L^2(D)$ error for $f = 0$: Crank-Nicolson scheme with $\Delta T = 10^{-2}$ and $\delta t = 10^{-3}$.

T^n	$\text{Rel}_{H_\kappa^1}^{\text{EW}}(T^n)$	$\text{Rel}_{H_\kappa^1}^0(T^n)$	$\text{Rel}_{H_\kappa^1}^1(T^n)$	$\text{Rel}_{H_\kappa^1}^2(T^n)$	$\text{Rel}_{H_\kappa^1}^3(T^n)$	$\text{Rel}_{H_\kappa^1}^4(T^n)$
0.01	7.0217	28.3350	16.7674	7.0138	7.0138	7.0138
0.02	7.0053	39.6766	31.9136	7.3167	7.0129	7.0129
0.03	7.0010	61.1794	51.3326	8.0179	7.0264	7.0138
0.04	7.0014	87.7871	76.1885	8.7646	7.0801	7.0154
0.05	7.0065	119.2332	106.9788	10.1730	7.1238	7.0207
0.06	7.0162	156.0967	144.4364	13.0098	7.1297	7.0285
0.07	7.0307	199.2282	189.6019	17.7065	7.1231	7.0341
0.08	7.0501	249.6645	243.7722	24.5026	7.1574	7.0358
0.09	7.0742	308.6303	308.4945	33.6707	7.3146	7.0357
0.10	7.1032	377.5617	385.5910	45.5892	7.7242	7.0368

Table 10: Convergence history of Algorithm 2 in relative $H_\kappa^1(D)$ error for $f = 0$: Crank-Nicolson scheme with $\Delta T = 10^{-2}$ and $\delta t = 10^{-3}$.

7 Conclusion

We propose in this paper a new efficient algorithm for parabolic problems with heterogeneous coefficients. This algorithm is named as the Wavelet-based Edge Multiscale Parareal (WEMP) Algorithm, which incorporates parareal algorithm into the Wavelet-based Edge Multiscale Finite Element Methods (WEMsFEMs). Therefore, it can handle parabolic problems with heterogeneous coefficients more efficiently if multiple processors are available. We derive the convergence rate of this algorithm, and verify its performance by several numerical tests. Future work includes the investigation of WEMP algorithm for time-fractional diffusion problems with heterogeneous coefficients.

References

- [1] G. Ariel, S. J. Kim, and R. Tsai. Parareal multiscale methods for highly oscillatory dynamical systems. *SIAM J. Sci. Comput.*, 38(6):A3540–A3564, 2016.
- [2] G. Bal. On the convergence and the stability of the parareal algorithm to solve partial differential equations. In *Domain decomposition methods in science and engineering*, pages 425–432. Springer, 2005.
- [3] G. Bal and Y. Maday. A “parareal” time discretization for non-linear PDE’s with application to the pricing of an American put. In *Recent developments in domain decomposition methods (Zürich, 2001)*, volume 23 of *Lect. Notes Comput. Sci. Eng.*, pages 189–202. Springer, Berlin, 2002.
- [4] L. Berlyand and H. Owhadi. Flux norm approach to finite dimensional homogenization approximations with non-separated scales and high contrast. *Arch. Ration. Mech. Anal.*, 198(2):677–721, 2010.
- [5] A. Blouza, L. Boudin, and S. M. Kaber. Parallel in time algorithms with reduction methods for solving chemical kinetics. *Commun. Appl. Math. Comput. Sci.*, 5(2):241–263, 2010.
- [6] A. J. Christlieb, C. B. Macdonald, and B. W. Ong. Parallel high-order integrators. *SIAM J. Sci. Comput.*, 32(2):818–835, 2010.

- [7] W. E and B. Engquist. The heterogeneous multiscale methods. *Commun. Math. Sci.*, 1(1):87–132, 2003.
- [8] Y. Efendiev, J. Galvis, and T. Hou. Generalized multiscale finite element methods. *J. Comput. Phys.*, 251:116–135, 2013.
- [9] L. C. Evans. *Partial Differential Equations*. American Mathematical Society, 2 edition, Mar. 2010.
- [10] R. D. Falgout, S. Friedhoff, T. V. Kolev, S. P. MacLachlan, and J. B. Schroder. Parallel time integration with multigrid. *SIAM J. Sci. Comput.*, 36(6):C635–C661, 2014.
- [11] C. Farhat and M. Chandesris. Time-decomposed parallel time-integrators: theory and feasibility studies for fluid, structure, and fluid-structure applications. *Internat. J. Numer. Methods Engrg.*, 58(9):1397–1434, 2003.
- [12] C. Farhat, J. Cortial, C. Dastillung, and H. Bavestrello. Time-parallel implicit integrators for the near-real-time prediction of linear structural dynamic responses. *Internat. J. Numer. Methods Engrg.*, 67(5):697–724, 2006.
- [13] P. F. Fischer, F. Hecht, and Y. Maday. A parareal in time semi-implicit approximation of the Navier-Stokes equations. In *Domain decomposition methods in science and engineering*, volume 40 of *Lect. Notes Comput. Sci. Eng.*, pages 433–440. Springer, Berlin, 2005.
- [14] S. Fu, E. Chung, and G. Li. Edge multiscale methods for elliptic problems with heterogeneous coefficients. *J. Comput. Phys.*, 369(1):228–242, 2019.
- [15] S. Fu, G. Li, R. Craster, and S. Guenneau. Wavelet-based edge multiscale finite element method for helmholtz problems in perforated domains. *Submitted*, 2019.
- [16] M. J. Gander and E. Hairer. Nonlinear convergence analysis for the parareal algorithm. In *Domain decomposition methods in science and engineering XVII*, pages 45–56. Springer, 2008.
- [17] M. J. Gander, I. Kulchytska-Ruchka, I. Niyonzima, and S. Schöps. A new parareal algorithm for problems with discontinuous sources. *SIAM J. Sci. Comput.*, 41(2):B375–B395, 2019.
- [18] M. J. Gander, I. Kulchytska-Ruchka, and S. Schöps. A New Parareal Algorithm for Time-Periodic Problems with Discontinuous Inputs. *arXiv e-prints*, Oct. 2018.
- [19] T. Hou and X.-H. Wu. A multiscale finite element method for elliptic problems in composite materials and porous media. *J. Comput. Phys.*, 134(1):169–189, 1997.
- [20] T. Hughes, G. Feijóo, L. Mazzei, and J.-B. Quincy. The variational multiscale method—a paradigm for computational mechanics. *Comput. Methods Appl. Mech. Engrg.*, 166(1-2):3–24, 1998.
- [21] F. Legoll, T. Lelièvre, and G. Samaey. A micro-macro parareal algorithm: application to singularly perturbed ordinary differential equations. *SIAM J. Sci. Comput.*, 35(4):A1951–A1986, 2013.
- [22] G. Li. On the convergence rates of gmsfems for heterogeneous elliptic problems without oversampling techniques. *Multiscale Modeling & Simulation*, 17(2):593–619, 2019.

- [23] G. Li, D. Peterseim, and M. Schedensack. Error analysis of a variational multiscale stabilization for convection-dominated diffusion equations in two dimensions. *IMA J. Numer. Anal.*, 38(3):1229–1253, 2018.
- [24] J.-L. Lions, Y. Maday, and G. Turinici. Résolution d’EDP par un schéma en temps “pararéel”. *C. R. Acad. Sci. Paris Sér. I Math.*, 332(7):661–668, 2001.
- [25] Y. Liu and J. Hu. Modified propagators of parareal in time algorithm and application to Princeton ocean model. *Internat. J. Numer. Methods Fluids*, 57(12):1793–1804, 2008.
- [26] M. Luskin and R. Rannacher. On the smoothing property of the Crank-Nicolson scheme. *Applicable Anal.*, 14(2):117–135, 1982/83.
- [27] Y. Maday. Parareal in time algorithm for kinetic systems based on model reduction. In *High-dimensional partial differential equations in science and engineering*, volume 41 of *CRM Proc. Lecture Notes*, pages 183–194. Amer. Math. Soc., Providence, RI, 2007.
- [28] Y. Maday, J. Salomon, and G. Turinici. Monotonic parareal control for quantum systems. *SIAM J. Numer. Anal.*, 45(6):2468–2482, 2007.
- [29] A. Målqvist and D. Peterseim. Localization of elliptic multiscale problems. *Math. Comp.*, 83(290):2583–2603, 2014.
- [30] K. C. T. Strouboulis, I. Babuška. The design and analysis of the generalized finite element method. *Comput. Methods Appl. Mech. Engrg.*, 181:43–69, 2000.
- [31] V. Thomée. *Galerkin finite element methods for parabolic problems*, volume 1054. Springer, 2006.